

Galactic mass-to-light ratios with superfluid dark matter

T. Mistele¹, S. McGaugh², and S. Hossenfelder¹

- Frankfurt Institute for Advanced Studies, Ruth-Moufang-Str. 1, 60438 Frankfurt am Main, Germany e-mail: mistele@fias.uni-frankfurt.de
- ² Department of Astronomy, Case Western Reserve University, 10900 Euclid Avenue, Cleveland, OH 44106, USA

Received 28 January 2022 / Accepted 8 April 2022

ABSTRACT

Context. We make rotation curve fits to test the superfluid dark matter model.

Aims. In addition to verifying that the resulting fits match the rotation curve data reasonably well, we aim to evaluate how satisfactory they are with respect to two criteria, namely, how reasonable the resulting stellar mass-to-light ratios are and whether the fits end up in the regime of superfluid dark matter where the model resembles modified Newtonian dynamics (MOND).

Methods. We fitted the superfluid dark matter model to the rotation curves of 169 galaxies in the SPARC sample.

Results. We found that the mass-to-light ratios obtained with superfluid dark matter are generally acceptable in terms of stellar populations. However, the best-fit mass-to-light ratios have an unnatural dependence on the size of the galaxy in that giant galaxies have systematically lower mass-to-light ratios than dwarf galaxies. A second finding is that the superfluid often fits the rotation curves best in the regime where the superfluid's force cannot resemble that of MOND without adjusting a boundary condition separately for each galaxy. In that case, we can no longer expect superfluid dark matter to reproduce the phenomenologically observed scaling relations that make MOND appealing. If, on the other hand, we consider only solutions whose force approximates MOND well, then the total mass of the superfluid is in tension with gravitational lensing data.

Conclusions. We conclude that even the best fits with superfluid dark matter are still unsatisfactory for two reasons. First, the resulting stellar mass-to-light ratios show an unnatural trend with galaxy size. Second, the fits do not end up in the regime that automatically resembles MOND, and if we force the fits to do so, the total dark matter mass is in tension with strong lensing data.

Key words. galaxies: kinematics and dynamics – dark matter – gravitation – gravitational lensing: strong

1. Introduction

In 2015, Berezhiani & Khoury (2015) proposed a new hypothesis that combines features of cold dark matter (CDM) and modified Newtonian dynamics (MOND; Milgrom 1983a,b,c; Bekenstein & Milgrom 1984): superfluid dark matter (SFDM). In SFDM, dark matter is composed of a light (on the order of eV) scalar field that can condense to a superfluid. In the superfluid phase, phonons mediate a force that is similar to the force of MOND. This hypothesis has since passed several observational tests (Berezhiani et al. 2018; Hossenfelder & Mistele 2019, 2020).

However, it was recently found that SFDM needs about 20% less baryonic mass than MOND to fit the Milky Way rotation curve at $R \leq 25 \,\mathrm{kpc}$ (Hossenfelder & Mistele 2020). Though a modest effect, this underestimates the stellar mass required by microlensing (Wegg et al. 2017). It also underestimates the amplitude of the spiral structure required to reconcile the Galactic rotation curve measured independently by stars and gas (McGaugh 2019). This offset is similar to that found for emergent gravity (Verlinde 2017) by Lelli et al. (2017a), which shares some properties of SFDM, thus raising the prospect that it might be a general trend. Consequently, SFDM may require a systematically smaller stellar mass-to-light ratio (M/L_*) than MOND. Since MOND generally agrees with the M/L_* expected from stellar population synthesis (SPS) models (McGaugh 2004), such a systematic trend can be problematic for SFDM. To investigate this, we fitted SFDM to the Spitzer Photometry and Accurate Rotation Curves (SPARC) data (Lelli et al. 2016) with M/L_* as a fitting parameter.

2. Models

Four parameters are required for SFDM; we used the fiducial values from Berezhiani et al. (2018), $m = 1 \,\text{eV}$, $\Lambda = 0.05 \,\text{meV}$, $\alpha = 5.7$, and $\beta = 2$. We kept those parameters fixed during our analysis. In Appendix D.2.6, we argue that our conclusions are generally robust against variations in these parameters.

The total acceleration inside the superfluid core of a galaxy is $a_{\text{tot}} = a_{\theta} + a_b + a_{\text{SF}}$, where a_{θ} is the acceleration created by the phonon force, a_{SF} the acceleration stemming from the normal gravitational attraction of the superfluid, and a_b that stemming from the mass of the baryons. The position dependence of those accelerations is determined by the SFDM equations of motion and the distribution of baryonic mass. At a transition radius where the superfluid condensate is estimated to break down, one matches the superfluid core to a Navarro-Frenk-White (NFW) halo (Berezhiani et al. 2018).

From integrating the standard Poisson equation including the superfluid's energy density ρ_{SF} as a source term, one obtains $\hat{\mu}(x) = \mu_{nr} - m\phi_N(x)$, where μ_{nr} is the chemical potential and $\phi_N(x)$ is the Newtonian gravitational potential. The gradient of $\phi_N(x)$ gives $a_b + a_{SF}$. In the so-called no-curl approximation, one obtains the phonon force, a_θ , as an algebraic function of a_b and $\varepsilon_*(x)$ (see Appendix A.1),

$$\varepsilon_*(\mathbf{x}) := \frac{2m^2}{\alpha M_{\rm Pl}|\mathbf{a}_b(\mathbf{x})|} \frac{\hat{\mu}(\mathbf{x})}{m},\tag{1}$$

where $M_{\rm Pl}$ is the Planck mass (it enters through Newton's constant). The quantity $\varepsilon_*(x)$ controls how closely SFDM resembles MOND. We refer to $|\varepsilon_*| \ll 1$ as the MOND limit and to

 $|\varepsilon_*| = O(1)$ as the pseudo-MOND limit. In the MOND limit and assuming the no-curl approximation, the phonon force points into the same direction as a_b with magnitude $a_\theta = \sqrt{a_0 a_b}$. Here, $a_0 = \alpha^3 \Lambda^2/M_{\rm Pl}$ is the acceleration scale below which the phonon force becomes important compared to a_b . At larger accelerations, it is subdominant. This gives a typical MOND-like total acceleration $a_{\rm tot}$, at least as long as $a_{\rm SF}$ stays negligible. Usually, $a_{\rm SF}$ is indeed negligible in the proper MOND limit $|\varepsilon_*| \ll 1$ but less so in the pseudo-MOND limit $|\varepsilon_*| = O(1)$. More details on the definition and rationale behind these limits are in Appendix A (see also Mistele 2021). The actual value of ε_* depends on the baryonic mass distribution and a boundary condition needed to solve the equations of motion.

A big advantage of MOND is that galactic scaling relations such as the radial acceleration relation (RAR; Lelli et al. 2017b) arise automatically with no intrinsic scatter. The same goes for SFDM in the MOND limit $|\varepsilon_*| \ll 1$. In this limit, SFDM predicts a tight RAR irrespective of the precise value of the boundary condition. This is different outside the MOND limit where the total acceleration $a_{\rm tot}$ depends sensitively on the choice of the boundary condition. Thus, outside the MOND limit, scaling relations such as the RAR can arise only by adjusting this boundary condition separately for each galaxy. Otherwise, increased scatter and systematic deviations are likely.

In principle, it might be possible that galaxy formation selects the right boundary condition for each galaxy to produce a tight RAR even outside the MOND limit. However, then SFDM loses one of its main advantages over Λ CDM and one might as well stick with Λ CDM.

We compared SFDM to MOND using one of the standard interpolation functions (Lelli et al. 2017b),

$$\nu_e(y) = \frac{1}{1 - e^{-\sqrt{y}}},\tag{2}$$

where $y=|a_b|/a_0$ and a_0 is the one free parameter in MOND. In SFDM the interpolation function is slower to reach its limits for large and small y. Also, usually a_0 is chosen smaller in SFDM compared to MOND to account for the presence of $a_{\rm SF}$ (Berezhiani et al. 2018). For MOND, we adopt $a_0^{\rm MOND} \approx 1.2 \times 10^{-10} \, {\rm m \, s^{-2}}$ from Lelli et al. (2017b). For SFDM, the fiducial parameters from Berezhiani et al. (2018) give $a_0^{\rm SFDM} \approx 0.87 \times 10^{-10} \, {\rm m \, s^{-2}}$.

To check how sensitive our results are to the particular theoretical realization of SFDM, we included the two-field model from Mistele (2021). In this two-field model, the phenomenology on galactic scales is similar to standard SFDM, but it has the advantages that (a) it does not require ad-hoc finite-temperature corrections for stability, (b) its phonon force is always close to its MOND-limit, and (c) the superfluid can remain in equilibrium much longer than galactic timescales. Both models are described in more detail in Appendix A.

3. Data

We took the observed rotation velocity $V_{\rm obs}$ directly from SPARC (Lelli et al. 2016). To find the best SFDM fit, we then needed the baryonic energy density $\rho_b(R,z)$ because it is a source for the equation of motion of the superfluid. For this, we used updated high-resolution mass models including resolved gas surface density profiles for 169 of the 175 SPARC galaxies (Lelli 2021, priv. comm.). We excluded the six galaxies that lack radial profiles for the gas distribution.

These mass models provide surface densities Σ for the bulge, the stellar disk, and the HI disk of each galaxy for a discrete set of positions starting at R=0. We linearly interpolated the data points and assumed zero surface density outside the outermost surface density data point. This gives a simple, data-compatible approximation for the density distribution at all radii.

For the bulge, we assumed spherical symmetry and extracted its energy density from its surface density using an Abel transform.

$$\rho_{\text{bulge}}(r) = -\frac{1}{\pi} \int_0^\infty d\bar{r} \frac{\Sigma'_{\text{bulge}}(\sqrt{\bar{r}^2 + r^2})}{\sqrt{\bar{r}^2 + r^2}}.$$
 (3)

For the stellar disk, we assumed a scale height, h_* , of (Lelli et al. 2016)

$$h_* = 0.196 \cdot (R_{\text{disk}}[\text{kpc}])^{0.633} \text{ kpc},$$
 (4)

where R_{disk} is the disk scale length from SPARC. Again, we used a linear interpolation of the SPARC surface brightness data points.

For the gas disk we did the same as for the stellar disk, except that in this case we assumed a fixed scale height, $h_g = 0.130 \,\mathrm{kpc}$. This is the same scale height used in Hossenfelder & Mistele (2020). We do not expect this choice of scale height to significantly affect the results. To account for the non-HI gas, we multiplied the HI surface density by 1.4 (McGaugh et al. 2020).

4. Method

Solutions of the equations of motion can be parameterized by one boundary condition, $\varepsilon := \varepsilon_*(R_{\rm mid})$, where $R_{\rm mid} := (R_{\rm min} + R_{\rm max})/2$, and $R_{\rm min}$ ($R_{\rm max}$) is the smallest (largest) radius with a rotation curve data point. The value of ε quantifies how closely the phonon force resembles a MOND force in the middle of the observed rotation curve.

In our fitting procedure, we kept $V_{\rm obs}$ and the fiducial model parameters of SFDM fixed, but we allowed a common factor, Q_* , to adjust the stellar disk and bulge M/L_* relative to the nominal stellar population values in the *Spitzer* [3.6] band $(M/L_*)_{\rm disk} = 0.5$ and $(M/L_*)_{\rm bulge} = 0.7$ (Lelli et al. 2017b),

$$\rho_b(R, z) = \rho_{\text{gas}}(R, z) + 0.5 \cdot Q_* \cdot \rho_*(R, z) + 0.7 \cdot Q_* \cdot \rho_{\text{bulge}}(\sqrt{R^2 + z^2}).$$
 (5)

Using this total baryonic energy density, we solved the SFDM equations of motion for different boundary conditions. From that we then obtained the expected rotation curve.

We assume that all rotation curve data points are within the superfluid core; otherwise, rotation curves cannot be automatically MOND-like since the MOND-like phonon force is active only inside the superfluid. In our fits, we took the superfluid phase to end only when its energy density reaches zero. That is, we only required that $\varepsilon_*(x)$ (see Eq. (1)) is larger than an algebraic minimum value ε_{\min} everywhere within the superfluid. This minimum value is reached when ρ_{SF} vanishes and (for the case of $\beta=2$) is given by $\varepsilon_{\min}=-\sqrt{3/32}\approx-0.31$.

For the best fits, we then checked whether all data points lie within the superfluid core according to a different criterion based on thermal equilibrium. It turns out that for 31 of the 169 galaxies this is not the case. However, this criterion for the value of the transition radius to the NFW halo is quite ad hoc. We therefore do not discard these solutions, though we checked that they do not alter the main conclusions (see also Appendix D.2.7).

Then we compared how well this rotation curve matches with the observed velocities, $V_{\rm obs}$, from SPARC. For this, we defined the best fit for each galaxy as that with the smallest χ^2 ,

$$\chi^{2} = \frac{1}{N - f} \sum_{R} \frac{(V_{\text{obs}}(R) - V_{c}(R))^{2}}{\sigma_{V_{\text{obs}}}^{2}(R)}.$$
 (6)

Here, N is the number of data points in the galaxy, f=2 is the number of fit parameters $(Q_* \text{ and } \varepsilon)$, $\sigma_{V_{\text{obs}}}$ is the uncertainty on the velocity V_{obs} from SPARC, $V_c(R)$ is the calculated rotation curve in SFDM, and the sum is over the data points at radius R.

We minimized χ^2 for

$$10^{-2} \le Q_* \le 15,\tag{7}$$

$$10^{-2} \le (\varepsilon - \varepsilon_{\min}) \le 10^4. \tag{8}$$

In our fit code, we scanned values of $\log_{10}(Q_*)$ and $\log_{10}(\varepsilon - \varepsilon_{\min})$.

In the SPARC data, the Newtonian acceleration due to gas sometimes points outward from the galactic center, not toward it, because of a hole in the HI data, possibly due to a transition from atomic to molecular gas. Usually, such a negative gas contribution is countered by the positive contributions from the stellar disk and the bulge and does not pose a problem. When this is not the case, there is technically no stable circular orbit so we cannot calculate a rotation curve. When this happened, we omitted those data points when calculating χ^2 .

As a cross-check and as a comparison for SFDM, we also fitted the RAR to the SPARC data, that is, we fitted the SPARC data with MOND assuming no curl term and the exponential interpolation function ν_e (Lelli et al. 2017b). In this case, we have only one free fit parameter, Q_* , and consequently, when calculating χ^2 , we set f=1. We describe our fitting and calculation methods in more detail in Appendix C.

5. Results

The result of our MOND fit is similar to that of Li et al. (2018), which also fitted the RAR to SPARC galaxies. The major difference is that Li et al. (2018) used a Markov chain Monte Carlo (MCMC) procedure with Gaussian priors, while we used a simple parameter scan to minimize χ^2 . We also did not vary distance and inclination and did not separately vary the mass-to-light ratio of the stellar disk and the bulge. As a consequence of this simplified fitting procedure, our distribution of best-fit M/L_* has more outliers and looks less Gaussian than that of Li et al. (2018).

Still, our median best-fit stellar mass-to-light ratios and the best-fit χ^2 values are similar to those from Li et al. (2018). The median stellar disk M/L_* is 0.39. When we restrict ourselves to galaxies with high quality data (q=1), this becomes 0.47, very similar to the 0.50 from Li et al. (2018). We show the χ^2 cumulative distribution function (CDF) in Fig. 1, which is also in reasonable agreement with Li et al. (2018).

In Fig. 2 one sees that some galaxies end up at the minimum stellar mass-to-light ratio allowed in our fitting method, corresponding to $Q_* \approx 0.01$. If we do not restrict ourselves to q=1, this peak at $Q_* \approx 0.01$ is even more pronounced. As discussed in Appendix D.1, this is an artifact of our fitting procedure and can be ignored in what follows.

5.1. MOND versus SFDM

Figure 2 shows the best-fit Q_* for the 97 galaxies with q=1. Contrary to what one might naively expect from the Milky Way

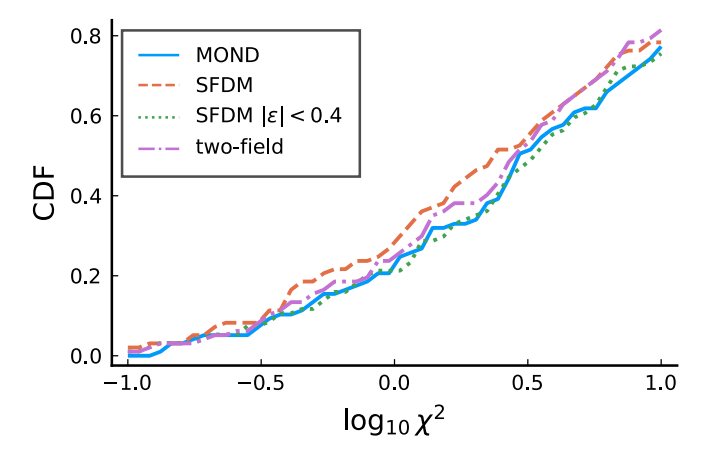


Fig. 1. Best-fit χ^2 cumulative distribution functions for the q=1 galaxies for different models.

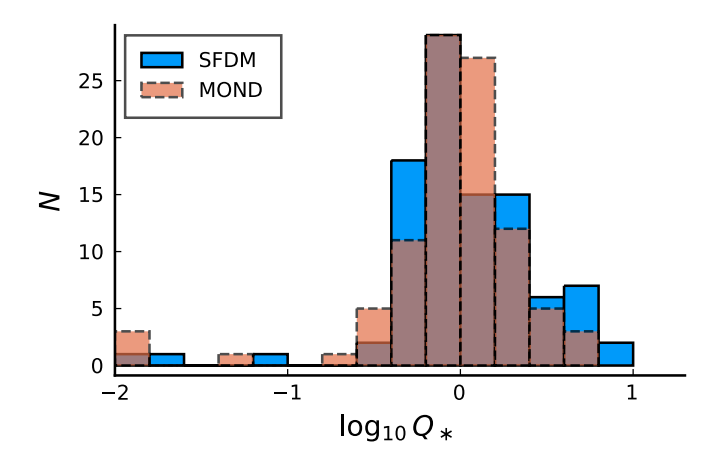


Fig. 2. Histograms of the best-fit Q_* values for the SFDM and MOND fits restricted to the q=1 galaxies.

result (Hossenfelder & Mistele 2019), the SFDM fits do not have significantly smaller Q_* than the MOND fits. Indeed, the median Q_* for the q = 1 galaxies is about 4% larger than for MOND.

One reason for this is that for many galaxies the superfluid is not in the MOND limit $|\varepsilon| \ll 1$, as one sees from Fig. 3. We theoretically explain why going outside the MOND limit allows for larger M/L_* in Appendix B.2. To confirm this, we did the fits again but required that the galaxies are in the MOND limit, $|\varepsilon| < 0.4$. For the rationale behind the precise value 0.4, please refer to Appendix D.2.3. The resulting Q_* values are shown in Fig. 4.

As one can see from Fig. 1, the fits with the requirement $|\varepsilon| < 0.4$ are not much worse than those without. The averaged Q_* is now smaller than in MOND; for the q=1 galaxies, the median stellar disk M/L_* is about 10% smaller than for MOND. This confirms superfluids outside the MOND limit as one reason for the large Q_* values in SFDM (see also Appendix D.2.2).

Another reason why SFDM does not universally give smaller Q_* than MOND is that the best-fit Q_* depends on the type of galaxy. In SFDM, Q_* is systematically smaller for galaxies with relatively large accelerations a_b , but not for those with small accelerations. This can be seen, for example, in the right panel of Fig. 5, which shows the best-fit Q_* of each galaxy in SFDM relative to the best-fit Q_* for MOND as a function of the observed asymptotic rotation velocity, $V_{\rm flat}$. A larger $V_{\rm flat}$ is associated with larger accelerations – this is, where SFDM systematically gives smaller Q_* than MOND. There are similar trends for

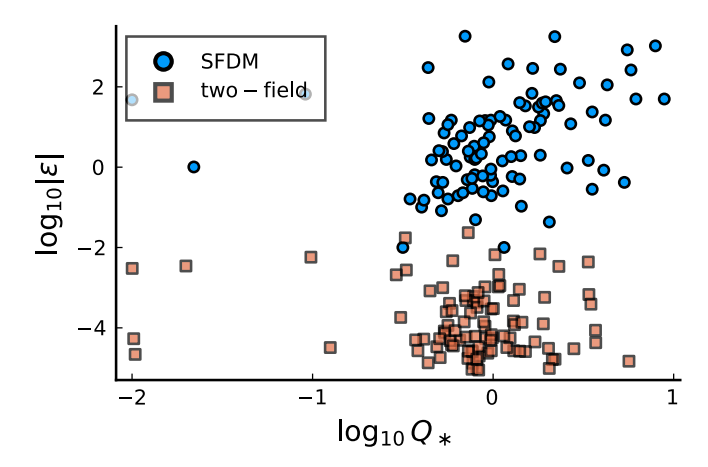


Fig. 3. Best-fit ε values versus the best-fit Q_* values for the q=1 galaxies. We show $\log_{10} |\varepsilon|$ rather than $\log_{10} |\varepsilon - \varepsilon_{\min}|$ to show how many galaxies end up in the MOND limit (corresponding to $|\varepsilon_*| \ll 1$) rather than how many galaxies end up close to $\rho_{\rm SF}=0$ (corresponding to $|\varepsilon_*-\varepsilon_{\min}|\ll 1$). For standard SFDM, the correlation coefficient is r=0.28.

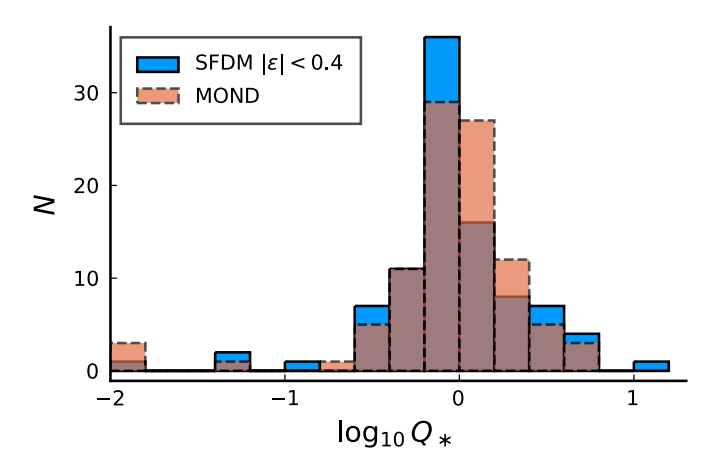


Fig. 4. Same as Fig. 2 but for SFDM restricted to $|\varepsilon| < 0.4$.

surface brightness and the gas fraction; both also correlate with the accelerations a_b (see Appendix D.2.4 for more details).

The reason for this trend is that the smaller a_0 value of SFDM makes the acceleration $\sqrt{a_0a_b}$ smaller than in MOND. This acceleration $\sqrt{a_0a_b}$ is dominant at small a_b , so that SFDM needs more baryonic mass than MOND to get the same total acceleration (at least if $a_{\rm SF}$ is negligible). This is explained in more detail in Appendix B.1.

This trend in $Q_*/Q_*^{\rm MOND}$ shows not only how SFDM is different from MOND but also how SFDM does not comply with expectations from SPS models. The general idea is that MOND is known to be in good agreement with the expectations of SPS (Sanders 1996; Sanders & Verheijen 1998; McGaugh 2004, 2020), so any systematic trend in $Q_*/Q_*^{\rm MOND}$ is potentially problematic.

In our case, both the MOND and the SFDM fits show increased scatter in Q_* for small galaxies. This is shown in the left panel of Fig. 5. One reason for the increased scatter is that the data for smaller galaxies is generally of lower quality. Another reason is that these galaxies tend to be gas-dominated, in which case adjusting Q_* has only a small effect on the overall fit. Consequently, larger changes in Q_* are needed to impact the fit quality. Indeed, the scatter increases dramatically at precisely the

scale where gas typically begins to dominate the mass budget (McGaugh 2011; Lelli 2022).

The SFDM fits show an upward trend in Q_* for small galaxies. This corresponds to the upward trend in Q_*/Q_*^{MOND} shown in the right panel of Fig. 5. The problem is that such trends of the stellar M/L_* with galaxy properties are not expected from SPS models for the late type galaxies that compose the SPARC sample. If anything, we expect the stellar M/L_* to increase with mass (e.g., Bell & de Jong 2001), opposite the sense of the trend found here. Indeed, we utilize the near-infrared Spitzer [3.6] band specifically to minimize variations in the mass-to-light ratio. In the most recent stellar population models of late type galaxies (e.g., Schombert et al. 2019, 2022), accounting for the shape of the stellar metallicity distribution tends to counteract the modest effect of stellar age in the near-infrared, leading to the expectation of a nearly constant M/L_* .

Given our simplistic fitting procedure, Fig. 5, left, alone may or may not be convincing evidence for a systematic trend in Q_* . Still, our fitting procedure is well suited to identify relative differences between MOND and SFDM, and we have a good theoretical understanding of this difference. Thus, we expect the trends in our best-fit Q_*/Q_*^{MOND} to be robust. Since Q_*^{MOND} is known to be in good agreement with SPS expectations, we interpret the systematic trend seen in the right panel of Fig. 5 as a good indicator of trends in absolute Q_* revealing a tension between SFDM and SPS.

In Appendix D.3 we show how our fit results illustrate that only the MOND limit of SFDM can reproduce MOND-like galactic scaling relations such as the RAR without having to adjust the boundary condition ε separately for each galaxy.

5.2. Tension with strong lensing

Irrespective of the resulting M/L_* values, there is a price to pay for enforcing the MOND limit in SFDM. A MOND-like rotation curve in the MOND limit $|\varepsilon_*| \ll 1$ can only be achieved by reducing the acceleration created by the gravitational pull of the superfluid. As a result, the total dark matter mass in those galaxies, $M_{200}^{\rm DM}$, comes out to be quite small. Here, $M_{200}^{\rm DM}$ is the dark matter mass within the radius r_{200} where the mean dark matter density drops below $\rho_{200} = 200 \times 3H^2/(8\pi G)$ with the Hubble constant H. We adopt $H = 67.3\,{\rm km\,s^{-1}\,Mpc^{-1}}$.

A small $M_{200}^{\rm DM}$ is not a problem for fitting SFDM to the observed rotation curves, but it is a problem if one also wants to fit strong lensing data. Indeed, Hossenfelder & Mistele (2019) find that SFDM requires ratios $M_{200}^{\rm DM}/M_b \gtrsim 1000$ to fit strong lensing constraints, where M_b is the total baryonic mass. Requiring a rotation curve in the MOND limit $|\varepsilon_*| \ll 1$ for the SPARC galaxies produces average masses at least an order of magnitude smaller.

To illustrate the problem with strong lensing, we have in Fig. 6 plotted the (logarithm of) the total baryonic and the maximum possible total dark matter mass given our requirement $|\varepsilon| < 0.4$ in comparison to the values found in Hossenfelder & Mistele (2019). For this, we used $Q_* = 1$ for all SPARC galaxies because the precise stellar mass-to-light ratio is irrelevant here. "Maximum possible" here refers not only to the requirement $|\varepsilon| < 0.4$ but also to uncertainties in how to determine the radius where the superfluid core is matched to an NFW halo: We used the transition radius that gives the largest total dark matter mass (see Appendix D.4 for details).

The best SFDM fits to strong lensing data tend to have $M_b \gtrsim 10^{11} M_{\odot}$ and $M_{200}^{\rm DM}/M_b \gtrsim 1000$. In contrast, despite our generous NFW matching procedure, the SPARC galaxies with

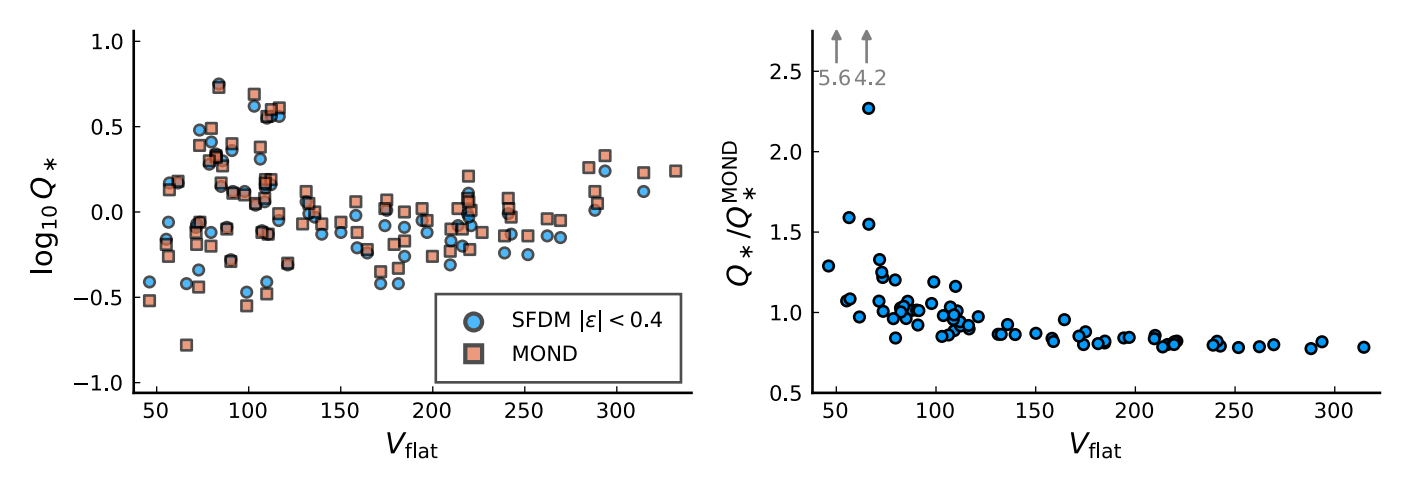


Fig. 5. Best-fit Q_* for SFDM restricted to the MOND limit ($|\varepsilon|$ < 0.4) and MOND as a function of the observed flat rotation velocity, V_{flat} , for the q=1 galaxies. For SFDM, some galaxies can barely satisfy the condition $|\varepsilon|$ < 0.4 and therefore give a bad fit to the data. Their best-fit Q_* is meaningless, and they are excluded from the SFDM fit results. Specifically, we exclude galaxies that have both $\varepsilon > 0.38$ and $\chi^2 > 100$. Left: best-fit Q_* for SFDM and MOND. As discussed at the beginning of Sect. 5, a few galaxies fall below the lower boundary of the plot. Their $(V_{\text{flat}} \cdot (\text{km s}^{-1})^{-1}, \log_{10} Q_*, \log_{10} Q_*^{\text{MOND}})$ values are (50.1, -1.25, -2.00), (65.2, -1.38, -2.00), and (66.3, -1.81, -2.00). Right: best-fit Q_* values for SFDM relative to those for MOND. Gray arrows indicate two outliers with relatively large Q_*/Q_*^{MOND} .

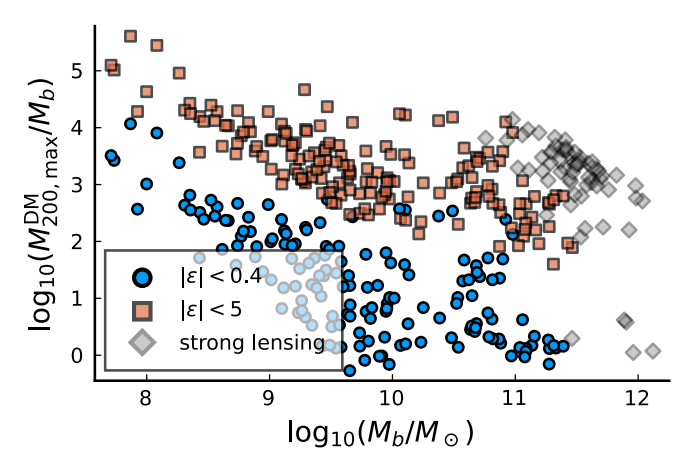


Fig. 6. Total baryonic mass, M_b , versus the upper bound, $M_{200,\text{max}}^{\text{DM}}/M_b$, of the ratio of the total dark matter mass, M_{200}^{DM} , and the baryonic mass for the SPARC galaxies. This is for $(M/L_*)_{\text{disk}}=0.5$ and $(M/L_*)_{\text{bulge}}=0.7$. The upper bound comes from the condition that the rotation curve is in the proper MOND limit ($|\varepsilon|<0.4$, blue circles) or at least the pseudo-MOND limit ($|\varepsilon|<5$, red squares). Also shown are the best-fit results from the strong lensing analysis of Hossenfelder & Mistele (2019), where we use their best-fit M_{200}^{DM} for the vertical axis.

 $M_b>10^{11}~M_\odot$ have $M_{200}^{\rm DM}/M_b<10$ when restricted to have rotation curves in the MOND limit $|\varepsilon|<0.4$. This is a stark contrast.

The SPARC galaxies do not reach baryonic masses quite as large as the lensing galaxies from Hossenfelder & Mistele (2019). But from Fig. 6 it seems clear that the trend goes into the wrong direction: The larger the galaxy, the smaller the maximum possible $M_{200}^{\rm DM}/M_b$ (given $|\varepsilon| < 0.4$).

The quoted values of $M_{200}^{\rm DM}/M_b$ for the strong lensing fits may seem high. But at least from a $\Lambda {\rm CDM}$ abundance matching perspective, these are actually expected due to the large baryonic masses of the lensing galaxies (Hossenfelder & Mistele 2019). Nevertheless, somewhat smaller ratios may be possible. The fitting procedure of Hossenfelder & Mistele (2019) did not aim to produce small $M_{200}^{\rm DM}/M_b$ values. It only aimed to simultaneously fit the observed Einstein radii and velocity dispersions of the lensing galaxies. Probably somewhat smaller $M_{200}^{\rm DM}/M_b$ ratios are

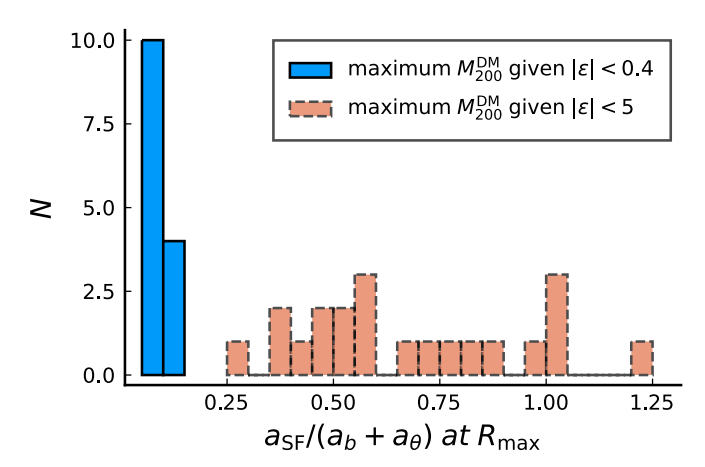


Fig. 7. Histogram of $a_{\rm SF}$ relative to a_b+a_θ at the last rotation curve data point at $R=R_{\rm max}$. This is for the maximum possible total dark matter mass, $M_{\rm 2DM}^{\rm DM}$, given the condition $|\varepsilon|<0.4$ (blue) and $|\varepsilon|<5$ (red). We take $Q_*=1$ for all galaxies and show only the galaxies with $M_b>10^{11}\,M_{\odot}$, relevant for strong lensing.

possible at the cost of somewhat worse fits of the Einstein radii and velocity dispersions. However, given the size of the discrepancy in Fig. 6, we do not expect that the proper MOND limit of SFDM can reasonably fit these data.

To study this closer, we did another calculation in which we allowed galaxies into the pseudo-MOND limit. Concretely, we redid the maximum $M_{200}^{\rm DM}/M_b$ calculation with the requirement $|\varepsilon| < 5$. The precise value 5 is again somewhat arbitrary. We explain why this is a pragmatic choice in Appendix D.2.3. We see from Fig. 6 that in the pseudo-MOND-limit galaxies with $M_b > 10^{11} \, M_{\odot}$ still have smaller total dark matter masses than what is required for strong lensing, although the problem is less severe than in the proper MOND limit. Somewhat worse but still acceptable fits to the strong lensing data might be able to ameliorate this.

The pseudo-MOND limit, however, is unsatisfactory for two reasons. First, it relies sensitively on ad hoc finite-temperature corrections of SFDM that may be unphysical. Second, the pseudo-MOND limit has the disadvantage that the acceleration

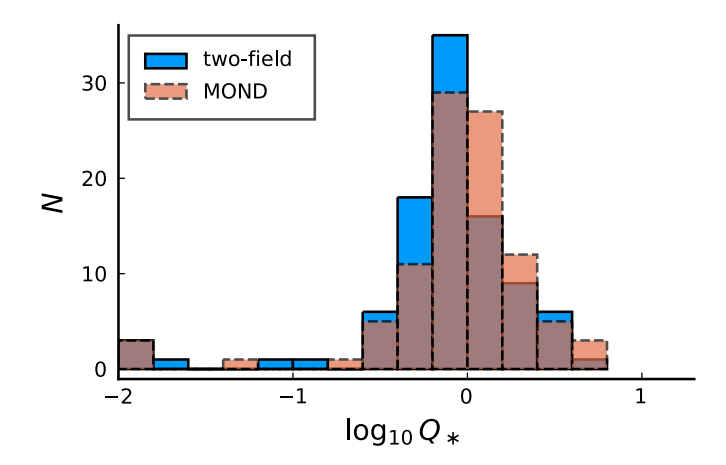


Fig. 8. Same as Fig. 2 but for two-field SFDM.

from the superfluid, $a_{\rm SF}$, can be significant. If $a_{\rm SF}$ is significant, we do not automatically get the MOND-type galactic scaling relations, since then the superfluid boundary condition must be adjusted for each galaxy to get the correct total acceleration. In this case, SFDM loses its advantage over CDM despite the phonon force being close to $\sqrt{a_0 a_b}$.

Figure 7 shows the size of $a_{\rm SF}$ relative to $a_b + a_\theta$ at the last rotation curve data point at $R = R_{\rm max}$, assuming the maximum total dark matter masses from Fig. 6. Indeed, for the pseudo-MOND limit, $a_{\rm SF}$ is significant for the galaxies with $M_b > 10^{11} \, M_\odot$ relevant for strong lensing. This is despite SFDM having a very cored dark matter profile. Thus, also with the pseudo-MOND limit, we cannot get MOND-like rotation curves and strong lensing at the same time.

5.3. Two-field SFDM

For two-field SFDM, the Q_* -distribution (Fig. 8) and the corresponding CDF (Fig. 1) are similar to those of standard SFDM. However, the two-field model is constructed so that it is easier for the phonon force to be close to the MOND-like value $\sqrt{a_0a_b}$. For this reason, the best fits for two-field SFDM all have $|\varepsilon_*| \ll 1$, as expected (Fig. 3). Only for two galaxies (NGC 6789, UGC 0732) does ε_* become larger than 0.1. Its largest value is 0.36 for NGC 6789. That is, the acceleration $a_b + a_\theta$ is almost always close to the MOND-like value $a_b + \sqrt{a_0a_b}$ (see Appendix D.5 for more details).

Thus, two-field SFDM can easily have large dark matter masses and $|\varepsilon_*| \ll 1$ at the same time. It does not have the same problem with strong lensing as the proper MOND limit $|\varepsilon_*| \ll 1$ of standard SFDM. Two-field SFDM does, however, still have a problem with strong lensing similar to the pseudo-MOND limit of standard SFDM. Large total dark matter masses imply that the rotation curve receives significant corrections from the superfluid's gravitational pull $a_{\rm SF}$. This is despite two-field SFDM having, like standard SFDM, a very cored density profile. For this reason, large total dark matter masses imply systematically higher rotation curve velocities than MOND.

To illustrate this problem we depict in Fig. 9 the maximum possible total dark matter mass for the two-field model, given the requirement that a_{SF} is at most 30% as large as $a_b + a_\theta$ at the last rotation curve data point at $R = R_{max}$ (see Appendix D.6). The scatter in the distribution is smaller in the two-field model because it depends less on the details of the baryonic matter distribution (see Appendix D.6). As one can see, in the two-

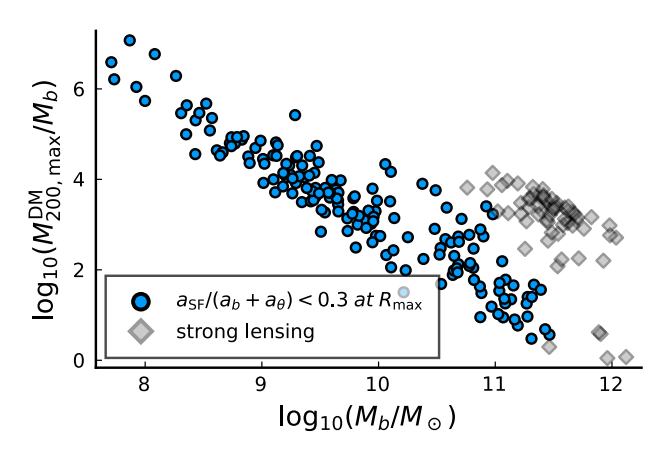


Fig. 9. Same as Fig. 6 but for the two-field model and with the requirement that a_{SF} is at most 30% as large as $a_b + a_\theta$ at the last rotation curve data point, R_{max} .

field model the discrepancy with the lensing data is weaker than for the proper MOND limit $|\varepsilon_*| \ll 1$ of standard SFDM, but still present. Avoiding this tension with the lensing data would require rotation curves that are even less MOND-like. Whether or not somewhat worse but still acceptable fits to the strong lensing data could ameliorate this problem requires further investigation.

6. Conclusion

We have found that it is difficult to reproduce the achievements of MOND with the models that have so far been proposed for SFDM.

Acknowledgements. This work was supported by the DFG (German Research Foundation) under grant number HO 2601/8-1 together with the joint NSF grant PHY-1911909.

References

```
Bekenstein, J., & Milgrom, M. 1984, ApJ, 286, 7
Bell, E. F., & de Jong, R. S. 2001, ApJ, 550, 212
Berezhiani, L., & Khoury, J. 2015, Phys. Rev. D, 92
Berezhiani, L., Famaey, B., & Khoury, J. 2018, JCAP, 1809, 021
Boran, S., Desai, S., Kahya, E. O., & Woodard, R. P. 2018, Phys. Rev. D, 97
Hossenfelder, S., & Mistele, T. 2019, JCAP, 1902, 001
Hossenfelder, S., & Mistele, T. 2020, MNRAS, 498, 3484
Lelli, F. 2022, Nat. Astron., 6, 35
Lelli, F., McGaugh, S. S., & Schombert, J. M. 2016, AJ, 152, 157
Lelli, F., McGaugh, S. S., & Schombert, J. M. 2017a, MNRAS, 468, L68
Lelli, F., McGaugh, S. S., Schombert, J. M., & Pawlowski, M. S. 2017b, ApJ,
   836, 152
Li, P., Lelli, F., McGaugh, S., & Schombert, J. 2018, A&A, 615, A3
McGaugh, S. S. 2004, ApJ, 609, 652
McGaugh, S. S. 2011, Phys. Rev. Lett., 106
McGaugh, S. 2019, ApJ, 885, 87
McGaugh, S. 2020, Galaxies, 8, 35
McGaugh, S. S., Lelli, F., & Schombert, J. M. 2020, Res. Notes Am. Astron.
   Soc., 4, 45
Milgrom, M. 1983a, ApJ, 270, 371
Milgrom, M. 1983b, ApJ, 270, 365
Milgrom, M. 1983c, ApJ, 270, 384
Mistele, T. 2021, JCAP, 2021, 025
Portail, M., Gerhard, O., Wegg, C., & Ness, M. 2017, MNRAS, 465, 1621
Sanders, R. H. 1996, ApJ, 473, 117
Sanders, R. H. 2018, Int. J. Mod. Phys. D, 27, 14
Sanders, R. H., & Verheijen, M. A. W. 1998, ApJ, 503, 97
Schombert, J., McGaugh, S., & Lelli, F. 2019, MNRAS, 483, 1496
Schombert, J., McGaugh, S., & Lelli, F. 2022, AJ, 163, 154
Verlinde, E. 2017, SciPost Phys., 2, 016
Wegg, C., Gerhard, O., & Portail, M. 2017, ApJ, 843, L5
```

Appendix A: The models

Here, we introduce both the original SFDM model from Berezhiani & Khoury (2015) and the two-field model from Mistele (2021) in more detail.

A.1. Standard SFDM

In standard SFDM, in an equilibrium superfluid core of a galaxy, the phonon field, θ , is determined by the equation (Berezhiani et al. 2018)

$$\nabla \left(\frac{(\nabla \theta)^2 + 2m(\frac{2\beta}{3} - 1)\hat{\mu}}{\sqrt{(\nabla \theta)^2 + 2m(\beta - 1)\hat{\mu}}} \nabla \theta \right) = \frac{\alpha}{2M_{\text{Pl}}} \rho_b, \tag{A.1}$$

and the field $\hat{\mu}$ is determined by the Poisson equation

$$\Delta\left(-\frac{\hat{\mu}}{m}\right) = 4\pi G \left(\rho_b + \rho_{\rm SF}\left[\hat{\mu}, \nabla \theta\right]\right),\tag{A.2}$$

with the superfluid energy density, $ho_{\rm SF}$,

$$\rho_{\rm SF}[\hat{\mu}, \nabla \theta] = \frac{2\sqrt{2}}{3} m^{5/2} \Lambda \frac{3(\beta - 1)\hat{\mu} + (3 - \beta)\frac{(\nabla \theta)^2}{2m}}{\sqrt{(\beta - 1)\hat{\mu} + \frac{(\nabla \theta)^2}{2m}}}.$$
 (A.3)

Here, m, Λ , and α are model parameters. The quantity $\hat{\mu}(x) = \mu_{\rm nr} - m\phi_N(x)$ is a combination of the (constant) non-relativistic chemical potential $\mu_{\rm nr}$ and the Newtonian gravitational potential $\phi_N(x)$. It controls how much the superfluid weighs, depending on a boundary condition (see Appendix C.2). The parameter β parametrizes finite-temperature corrections, which are needed to avoid an instability (Berezhiani & Khoury 2015). The phonon force a_θ is given by

$$\boldsymbol{a}_{\theta} = -\frac{\alpha \Lambda}{M_{\rm Pl}} \boldsymbol{\nabla} \theta. \tag{A.4}$$

We mainly used the no-curl approximation for the θ equation of motion. That is, for the solution of this equation, which is of the form $\nabla(g \cdot \nabla \theta) = a_b$ for some g, we assumed $g \nabla \theta = a_b$. This is a standard approximation in MOND and it works well also for SFDM (Hossenfelder & Mistele 2020).

In the no-curl approximation, the quantity $\varepsilon_*(x)$ (see Eq. (1)) is useful. As we will see, it controls how closely SFDM resembles MOND. As discussed in Mistele (2021), we have

$$|\mathbf{a}_{\theta}| = \sqrt{a_0 |\mathbf{a}_b|} \cdot \sqrt{x_{\beta}(\varepsilon_*)},$$
 (A.5)

where

$$a_0 = \frac{\alpha^3 \Lambda^2}{M_{\rm Pl}} \tag{A.6}$$

and where $x_{\beta}(\varepsilon_*)$ is determined by the cubic equation

$$0 = x_{\beta}^{3} + 2\left(\frac{2\beta}{3} - 1\right)\varepsilon_{*} \cdot x_{\beta}^{2} + \left(\left(\frac{2\beta}{3} - 1\right)^{2}(\varepsilon_{*})^{2} - 1\right)x_{\beta} - (\beta - 1)\varepsilon_{*}.$$
(A.7)

That is, a_{θ} is an algebraic function of a_b and ε_* . This also allows us to write ρ_{SF} as a function of $|a_b|$ and ε_* ,

$$\rho_{\rm SF}(\varepsilon_*, |\boldsymbol{a}_b|) = \frac{2}{3} \frac{m^2}{\alpha} \sqrt{a_0 |\boldsymbol{a}_b|} M_{\rm Pl} \cdot f_{\beta}(\varepsilon_*), \tag{A.8}$$

where

$$f_{\beta}(\varepsilon_*) = \frac{x_{\beta}(\varepsilon_*)(3-\beta) + 3(\beta-1)\varepsilon_*}{\sqrt{x_{\beta}(\varepsilon_*) + (\beta-1)\varepsilon_*}}.$$
(A.9)

For both a_{θ} and ρ_{SF} , we have a prefactor proportional to $\sqrt{a_0a_b}$ multiplied by a function that depends on ε_* and β only. For later use, we record the expansion of this second function for small and large values of ε_* . For $|\varepsilon_*| \ll 1$, we have

$$\sqrt{x_{\beta}(\varepsilon_*)} = 1 + O(\varepsilon_*), \tag{A.10a}$$

$$f_{\beta}(\varepsilon_*) = (3 - \beta) + O(\varepsilon_*).$$
 (A.10b)

For $\varepsilon_* \gg 1$,

$$\sqrt{x_{\beta}(\varepsilon_*)} = \frac{\sqrt{\beta - 1}}{2\beta - 3} \frac{3}{\sqrt{\varepsilon_*}} + O(\varepsilon_*^{-3/2}), \qquad (A.11a)$$

$$f_{\beta}(\varepsilon_*) = 3\sqrt{\varepsilon_*}\sqrt{\beta - 1} + O(\varepsilon_*^{-3/2}).$$
 (A.11b)

In general, f_{β} is a monotonically increasing, concave function of ε_* (see Fig. A.2). The function $\sqrt{x_{\beta}}$ is not monotonic (see Fig. A.1).

To avoid a negative or imaginary ρ_{SF} as well as an instability, ε_* must be larger than some minimum value $\varepsilon_{*\min}$. Berezhiani & Khoury (2015) assumed $\hat{\mu} > 0$, corresponding to $\varepsilon_* > 0$, but this is not required from their Lagrangian. It is an assumption with unclear justification. Here, we were more generous to the model and allowed $\hat{\mu}$ to become negative as long as ρ_{SF} stays positive. The corresponding minimum value of ε_* is determined by $\rho_{SF} = 0$, which is equivalent to $f_{\beta}(\varepsilon_{*\min}) = 0$. For example.

$$\varepsilon_{*\min} = \begin{cases} -\frac{29}{31} \sqrt{\frac{15}{31}} \approx -0.65, & \beta = 1.55\\ -\frac{1}{4} \sqrt{\frac{3}{2}} \approx -0.31, & \beta = 2\\ 0, & \beta = 3 \end{cases}$$
 (A.12)

With Eq. (1), this translates into a minimum value for $\hat{\mu}/m$,

$$\frac{\hat{\mu}(\mathbf{x})}{m} > \varepsilon_{*\min} \frac{\alpha M_{\text{Pl}} |\mathbf{a}_b(\mathbf{x})|}{2m^2}.$$
(A.13)

A.1.1. MOND limit

In SFDM, the total acceleration inside the superfluid core of a galaxy can be written as

$$\boldsymbol{a}_{\text{tot}} = \boldsymbol{a}_{\theta} + \boldsymbol{a}_{b} + \boldsymbol{a}_{\text{SF}},\tag{A.14}$$

where a_{θ} is the acceleration created by the phonon force, a_{SF} the acceleration stemming from the normal gravitational attraction of the superfluid, and a_b that stemming from the mass of the baryons.

For SFDM to make sense, one needs the superfluid to at least approximately reproduce MOND rotation curves without being sensitive to the choice of the boundary condition ε . Otherwise, one does not get the observed MOND-like scaling relations without carefully adjusting the boundary condition separately for each galaxy. That is to say, without the MOND limit of SFDM, one might as well use CDM.

Rotation curves in SFDM approximate those in MOND when the total acceleration $a_{\rm tot}$ approximately has the form $a_b + \sqrt{a_0 a_b}$. This corresponds to two conditions. First, the phonon force a_θ must be close to $\sqrt{a_0 a_b}$. Second, the superfluid's gravitational pull $a_{\rm SF}$ must be negligible.

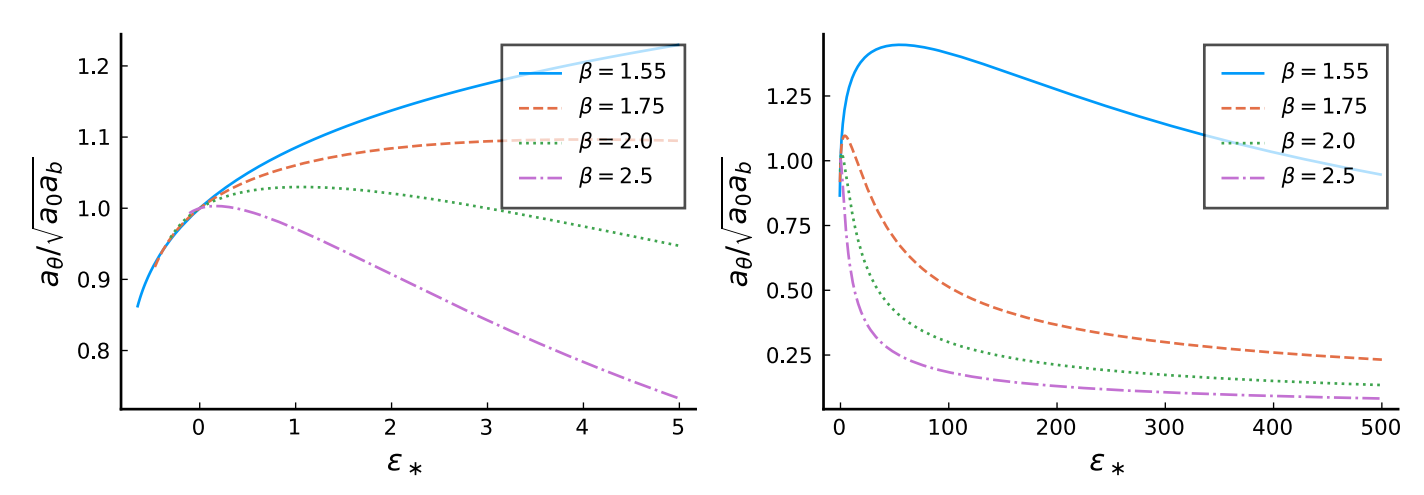


Fig. A.1. How close the phonon force, a_{θ} , is to its MOND limit value $\sqrt{a_0 a_b}$ as a function of ε_* . Left: For $\varepsilon_* < 5$ and for various values of the parameter, β , that parametrizes finite-temperature corrections. Right: Same but up to $\varepsilon_* = 500$.

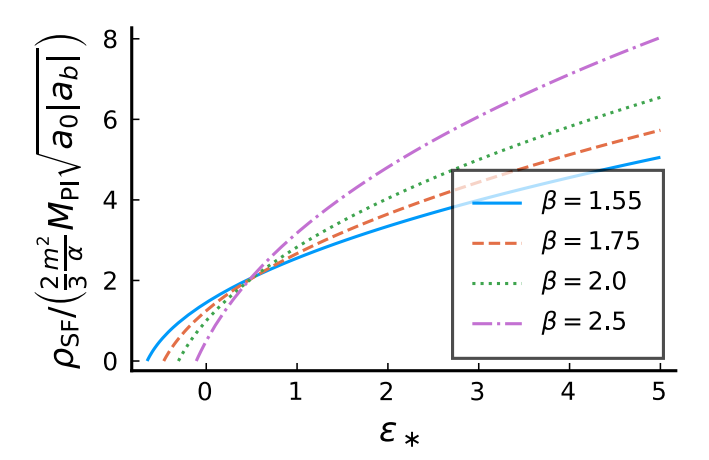


Fig. A.2. Function $f_{\beta}(\varepsilon_*) = \rho_{\rm SF} \cdot \left(\frac{2}{3} \frac{m^2}{a} M_{\rm Pl} \sqrt{a_0 |\boldsymbol{a}_b|}\right)^{-1}$ as a function of ε_* for different values of β . This is a concave, monotonically increasing function. It does not depend on any model parameters except β .

The numerical values of the model parameters and the boundary condition of the Poisson equation for $\hat{\mu}$ determine in which coordinate-range SFDM approximates MOND for a given baryonic mass distribution. Specifically, the MOND limit corresponds to $|\varepsilon_*(x)| \ll 1$. In this $|\varepsilon_*| \ll 1$ limit, both conditions to reproduce MOND rotation curves are automatically fulfilled: The phonon force is close to $\sqrt{a_0a_b}$ and the superfluid's gravitational pull $a_{\rm SF}$ is negligible. The phonon force is close to $\sqrt{a_0a_b}$ because, for $|\varepsilon_*| \ll 1$, the (no-curl version of) the phonon field equation Eq. (A.1) has the MOND-like form $|a_\theta|a_\theta=a_0a_b$. This corresponds to the small- $|\varepsilon_*|$ expansion $\sqrt{x_\beta}=1$ from Eq. (A.10a). We explicitly show that $a_{\rm SF}$ is negligible (i.e., that the second condition is fulfilled) at the end of this subsection.

However, even when ε_* is of order one, deviations of the phonon force from the MOND form $\sqrt{a_0a_b}$ remain within the percent range, at least for $\beta=2$ (see Fig. A.1). It will therefore in the following be handy to define a "pseudo-MOND limit," $\varepsilon_*=O(1)$. If this condition is fulfilled, the phonon field no longer satisfies a MOND-like equation, but the acceleration a_θ of an isolated galaxy is numerically still relatively close to $\sqrt{a_0a_b}$. One

difference to the proper MOND limit $|\varepsilon_*| \ll 1$ is that now the second condition for having MOND-like rotation curves is not automatically fulfilled. The superfluid's gravitational pull $a_{\rm SF}$ can be significant. So the observed scaling relations are fulfilled automatically only if $a_{\rm SF}$ stays sufficiently small, which needs to be checked separately for each solution.

A different problem with the pseudo-MOND limit is that it depends sensitively on the details of the ad hoc finite-temperature corrections introduced in Berezhiani & Khoury (2015) to avoid an instability. For example, the pseudo-MOND limit works only for β close to 2, as can be seen from Fig. A.1, left. Just as these ad hoc finite-temperature corrections, the pseudo-MOND limit may turn out to be unphysical.

It now remains to show that the superfluid's gravitational pull $a_{\rm SF}$ is negligible in the proper MOND limit $|\varepsilon_*| \ll 1$. For simplicity, we assume a point mass baryonic energy density, $\rho_b(x) = M_b \delta(x)$, which gives $a_b = G M_b / r^2$. Then, for $|\varepsilon_*| \ll 1$, we have $\rho_{\rm SF} \propto 1/r$ (see Eq. (A.10b)). The superfluid's mass is then

$$M_{\rm SF}(r) = M_b \cdot \left(\frac{r}{r_c}\right)^2,\tag{A.15}$$

where

$$r_c^{-2} = \sqrt{2\pi} \frac{m^2}{\alpha} \sqrt{\frac{a_0}{M_b}} \left(1 - \frac{\beta}{3} \right).$$
 (A.16)

We can now estimate the superfluid's gravitational pull a_{SF} compared to $a_b + a_\theta$. Roughly,

$$\frac{a_{\rm SF}}{a_b + a_\theta} \simeq \frac{(r/r_c)^2}{1 + r/r_{\rm MOND}},\tag{A.17}$$

with $r_{\text{MOND}} = \sqrt{GM_b/a_0}$. This ratio $a_{\text{SF}}/(a_b + a_\theta)$ can be larger than a fraction δ only at a radius r_δ that satisfies

$$r_{\delta} \gtrsim \delta \frac{r_{c}^{2}}{r_{\text{MOND}}} = \delta \cdot \frac{1}{\sqrt{2\pi G}} \frac{\alpha}{m^{2}} \frac{1}{1 - \frac{\beta}{3}} = 53 \,\text{kpc} \cdot \left(\frac{\delta}{10\%}\right), \quad (A.18)$$

where we used the fiducial numerical parameters from Berezhiani et al. (2018) for the last equality. That is, assuming the proper MOND limit $|\varepsilon_*| \ll 1$, the superfluid's mass becomes important only at radii larger than where rotation curves are measured.

¹ If a galaxy is not isolated, the phonon force may be different than in MOND because the external field effect will be different since θ does not satisfy a MOND-like equation.

A.1.2. Reaching the proper MOND limit

As already mentioned in Mistele (2021), reaching the proper MOND limit $|\varepsilon_*| \ll 1$ is not always possible. To avoid a negative $\rho_{\rm SF}$ there is a minimum value for $\hat{\mu}$ (see Eq. (A.13)). Typically, $\hat{\mu}$ is a decreasing function of galactocentric radius and the Poisson equation Eq. (A.2) tells us that $\hat{\mu}/m$ has a derivative of about $-GM/r^2$ where M includes both the baryonic and superfluid mass. Using the baryonic mass M_b as a lower bound on M then gives a lower bound on $\hat{\mu}/m$. Roughly, $\hat{\mu}/m \gtrsim \hat{\mu}_{\min}(r)/m + GM_b/r$. This translates into a rough lower bound on ε_* ,

$$\varepsilon_* \gtrsim \frac{2m^2r}{\alpha M_{\rm Pl}} + \varepsilon_{*\rm min} = 0.10 + 0.41 \cdot \left(\frac{r}{18\,{\rm kpc}} - 1\right),$$
 (A.19)

where we used $a_b = GM_b/r^2$ and the fiducial parameter values from Berezhiani et al. (2018).

Thus, small galaxies can easily reach the proper MOND limit $|\varepsilon_*| \ll 1$ over the whole range where their rotation curve is measured. One just needs to ensure that the superfluid mass is not too large, which is usually possible.

In contrast, larger galaxies sometimes struggle to satisfy the MOND limit condition $|\varepsilon_*| \ll 1$, even when the superfluid mass is as small as possible.

A.1.3. Naive upper bound on MOND limit dark matter mass

In Appendix A.1.1, we saw that being in the proper MOND limit $|\varepsilon_*| \ll 1$ restricts the superfluid's gravitational pull a_{SF} to be relatively small. Similarly, the MOND limit restricts the total dark matter mass to be relatively small, even if we include the noncondensed phase outside the superfluid core.

To see this, consider a galaxy with a superfluid core in the MOND limit $|\varepsilon_*| \ll 1$ and, for simplicity, assume a point mass baryonic mass distribution $\rho_b = M_b \delta(x)$. Then, the superfluid's mass is $M_{\rm SF} = M_b \cdot (r/r_c)^2$ (see Eq. (A.15)). In SFDM one usually assumes that the superfluid ends at some finite radius $r_{\rm NFW}$ where the superfluid's density is matched to that of an NFW halo. The total dark matter mass $M_{200}^{\rm DM}$ can be calculated from

$$M_{200}^{\rm DM} = \frac{4\pi}{3} r_{200}^3 \rho_{200} = M_{\rm SF}(r_{\rm NFW}) + M_{\rm NFW}(r_{\rm NFW}, r_{200}). \eqno(A.20)$$

Here, $M_{\rm NFW}$ denotes the mass of the NFW halo between the radii $r_{\rm NFW}$ and $r_{\rm 200}$. The NFW halo energy density falls off faster than the superfluid energy density (i.e., faster than 1/r). Thus, $M_{\rm NFW}$ grows slower than quadratically in r and we have the inequality

$$\frac{4\pi}{3}r_{200}^3\rho_{200} < M_b \left(\frac{r_{200}}{r_c}\right)^2. \tag{A.21}$$

That is,

$$\frac{r_{200}}{r_c} < \frac{M_b}{\frac{4\pi}{3}\rho_{200}r_c^3},\tag{A.22}$$

which is equivalent to

$$\frac{M_{200}^{\rm DM}}{M_b} < \left(\frac{M_b}{\frac{4\pi}{3}\rho_{200}r_c^3}\right)^2 = \frac{1}{\sqrt{2\pi}} \frac{9}{4} \frac{1}{\rho_{200}^2} \left(\frac{m^2}{\alpha}\right)^3 a_0^{3/2} \sqrt{M_b} \left(1 - \frac{\beta}{3}\right)^3. \quad (A.23)$$

Numerically, with the fiducial parameter values from Berezhiani et al. (2018) and $H = 67.3 \text{ km/(s \cdot Mpc)}$, this is

$$\frac{M_{200}^{\rm DM}}{M_b} < 0.9 \cdot \left(\frac{M_b}{10^{10} M_{\odot}}\right)^{1/2}. \tag{A.24}$$

This is too little for strong lensing even for very massive galaxies (see Appendix D.4). This upper bound is independent of the matching procedure to the NFW halo.

A.2. Two-field SFDM

Two-field SFDM contains two fields θ_+ and θ_- instead of just one field θ like standard SFDM (Mistele 2021). Still, in equilibrium only two nontrivial equations must be solved. One for θ_+ that carries the MOND-like force and one for the Newtonian gravitational potential ϕ_N . As in standard SFDM, we write the equations in terms of $\hat{\mu}/m$ where $\hat{\mu} = \mu_{\rm nr} - m\phi_N$, $\mu_{\rm nr}$ is the non-relativistic chemical potential, and m is the mass of the superfluid's constituent particles. Also, as in standard SFDM, the MOND limit of the phonon force is controlled by a quantity $\varepsilon_* = (2m^2/\alpha M_{\rm Pl} a_b)(\hat{\mu}/m)$. Thus, we use the same notation ε_* in both models.

This model has two contributions to the superfluid energy density, ρ_{SF+} and ρ_{SF-} . As discussed in Mistele (2021), usually ρ_{SF-} dominates. For our calculation below, we assumed that this is the case and neglected ρ_{SF+} . We verified that ρ_{SF+} is always at most 5% as large as ρ_{SF-} at $R=R_{mid}$ for the best fits

As in standard SFDM, we can get the phonon force from a no-curl approximation as a function of a_b and ε_* . We use the same notation a_θ as in standard SFDM. The quantity $\hat{\mu}/m$ is determined as in standard SFDM just with a different $\rho_{\rm SF}$. Concretely, we have in the no-curl approximation for an equilibrium superfluid

$$a_{\theta} = \sqrt{a_0 a_b} \sqrt{\sqrt{1 + \frac{\varepsilon_*^2}{4} + \frac{\varepsilon_*}{2}}}$$
 (A.25)

and

$$\rho_{\rm SF} = \rho_{\rm SF-} = \frac{2M_{\rm Pl}^2}{r_0^2} \frac{\hat{\mu}}{m},\tag{A.26}$$

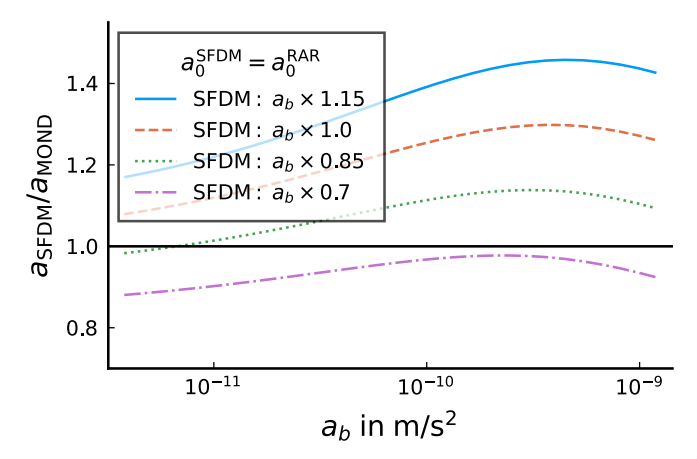
where r_0 is a parameter of the model.

We used the numerical parameter values from Mistele (2021). That is, $r_0 = 50\,\mathrm{kpc}$, $a_0 = 0.87 \cdot 10^{-10}\,\mathrm{m/s^2}$, and, unless stated otherwise, $\bar{a} = 10^{-12}\,\mathrm{m/s^2}$. The quantity m^2/α that enters ε_* is a combination of these, namely $m^2/\alpha = 10^{-7/2}\,(\bar{a}/a_0)^{1/4}(M_{\mathrm{Pl}}/r_0)$.

One difference to standard SFDM is that ε_* is almost always small so that the phonon force a_{θ} almost always has the MOND-like form $\sqrt{a_0a_b}$. But, in contrast to standard SFDM, a small $|\varepsilon_*|$ implies only that $a_{\theta} \approx \sqrt{a_0a_b}$, not that $a_{\rm SF}$ is small. Thus, even for $|\varepsilon_*| \ll 1$ one must check that $a_{\rm SF}$ is small in order to get MOND-like rotation curves. Otherwise, the total acceleration will be systematically larger than in MOND.

The energy density $\rho_{\rm SF}$ reaches zero for $\hat{\mu}=0$ in two-field SFDM (i.e. $\varepsilon_{*\rm min}=0$).

Appendix B: Comparison to MOND



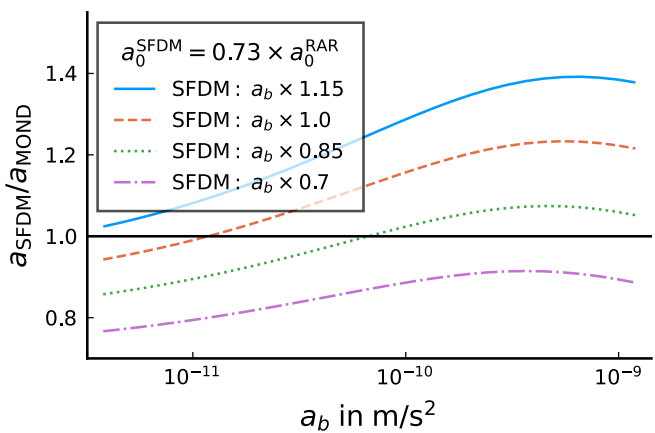


Fig. B.1. Ratio of the accelerations $a_{\rm SFDM}=a_b\,\nu_\theta(a_b/a_0)$ and $a_{\rm MOND}=a_b\,\nu_e(a_b/a_0)$ as a function of a_b . Top: With $a_{\rm SFDM}$ and $a_{\rm MOND}$ both using the same value for a_0 , namely $a_0=1.2\cdot 10^{-10}\,{\rm m/s^2}$, but with $a_{\rm SFDM}$ using a baryonic acceleration a_b that is multiplied by an overall factor relative to a_b in $a_{\rm MOND}$. Bottom: Same as top, but now $a_{\rm SFDM}$ and $a_{\rm MOND}$ use different values for a_0 , namely $a_0^{\rm SFDM}=0.87\cdot 10^{-10}\,{\rm m/s^2}$ and $a_0^{\rm RAR}=1.2\cdot 10^{-10}\,{\rm m/s^2}$, respectively.

B.1. Assuming the MOND limit of SFDM

For SFDM in the MOND limit we approximately have $a_{\text{tot}} \approx \sqrt{a_0 a_b} + a_b$, which, in MOND, would correspond to the interpolation function

$$\nu_{\theta}(y) = 1 + \frac{1}{\sqrt{y}},\tag{B.1}$$

with $y = a_b/a_0$.

At baryonic accelerations not much smaller or much larger than a_0 (i.e., y = O(1)), the additional acceleration from SFDM is significantly larger than what one obtains from standard MOND interpolation functions such as (Lelli et al. 2017b)

$$v_e(y) = \frac{1}{1 - e^{-\sqrt{y}}}. ag{B.2}$$

It is because of this difference in the interpolation functions that one may naively expect SFDM to require less baryonic mass than standard MOND models, at least in the MOND limit.

This is illustrated in Fig. B.1, top. The total acceleration in SFDM is always larger than in MOND, if both use the

same baryonic a_b . At intermediate accelerations ($a_b \sim a_0 \sim 10^{-10} \, \mathrm{m/s^2}$) the difference between MOND and SFDM is significant. This can be countered by making a_b in SFDM smaller, that is to say, by choosing a smaller mass-to-light ratio in SFDM than in MOND.

This discussion so far assumes the same a_0 for both SFDM and MOND. However, in practice, one usually chooses a somewhat smaller value for a_0 in SFDM. Indeed, Berezhiani et al. (2018) chose $a_0^{\rm SFDM} \approx 0.87 \cdot 10^{-10} \, \text{m/s}^2$, while MOND typically requires $a_0^{\rm RAR} \approx 1.2 \cdot 10^{-10} \, \text{m/s}^2$ (Lelli et al. 2017b). The motivation of Berezhiani et al. (2018) to choose a lower value is to take into account a possible effect of the superfluid's gravitational pull $a_{\rm SF}$. Indeed, at small accelerations a_b , the total acceleration in MOND is close to

$$\sqrt{a_0^{\text{RAR}}a_b},$$
 (B.3)

while in SFDM we have

$$\sqrt{a_0^{\text{SFDM}} a_b} + a_{\text{SF}}.\tag{B.4}$$

The smaller value of a_0 in SFDM allows us to get the same total acceleration even with a nonzero $a_{\rm SF}$. Numerically, the smaller a_0 value is compensated for when $a_{\rm SF}$ is about 0.15 $\sqrt{a_0^{\rm RAR} a_b}$.

Neglecting $a_{\rm SF}$, this smaller value of a_0 makes the total acceleration smaller, so it counters the need for less baryonic mass in SFDM. This is illustrated in Fig. B.1, bottom. The smaller a_0 value has the biggest impact at small accelerations a_b . At small accelerations, $a_b \ll a_0$, SFDM may even require more baryonic mass than MOND, at least if we neglect $a_{\rm SF}$. Indeed, $a_{\rm SF}$ is usually negligible in the proper MOND limit $|\varepsilon_*| \ll 1$, as discussed above. Thus, assuming the proper MOND limit, we expect to find systematically smaller M/L_* in SFDM than in MOND for galaxies with large a_b but not for galaxies with small a_b . This is roughly what we find in our fits below (see Appendix D.2.4).

B.2. Caveat: MOND limit

The above discussion applies in the MOND limit of SFDM. Outside this MOND limit, the phonon force does not necessarily have the form $a_{\theta} = \sqrt{a_0 a_b}$ and the superfluid's gravitational pull may not be negligible. For example, at $\varepsilon_* \to \infty$, we find that $a_{\theta} \propto 1/\sqrt{\varepsilon_*}$ (see Fig. A.1, right). That is, having a large ε_* makes a_{θ} small. A smaller acceleration may allow for larger baryonic masses. Thus, having galaxies end up at $\varepsilon_* \gg 1$ is a way to allow for relatively large mass-to-light ratios in our fits.

One might be skeptical of this argument for the following reason. The argument relies on the total acceleration a_{tot} becoming smaller for $\varepsilon_* \gg 1$. But this is not necessarily the case. A large ε_* does make a_θ smaller. But it is possible that the decrease in a_θ is compensated for by an increase in a_{SF} . Indeed, at large ε_* , the superfluid's energy density scales as

$$\rho_{\rm SF} \propto \sqrt{\hat{\mu}} \propto \sqrt{\varepsilon_* a_b}.$$
(B.5)

Thus, at fixed a_b , a larger ε_* makes the superfluid heavier and thus $a_{\rm SF}$ larger. For $\varepsilon_* \to \infty$, the acceleration $a_{\rm SF}$ can become arbitrarily large. Thus, the total acceleration does not become smaller for $\varepsilon_* \to \infty$, despite the smaller phonon acceleration a_θ .

Still, in practice there is a significant window of large values of ε_* where the total acceleration does become smaller. To see this explicitly, expand for large large ε_* . Then, roughly, $a_{\rm tot}$ scales with ε_* as

$$a_b + 3\sqrt{a_0a_b}\frac{\sqrt{\beta - 1}}{2\beta - 3}\left(\frac{1}{\sqrt{\varepsilon_*}} + \sqrt{\varepsilon_*} \cdot \frac{2\beta - 3}{3 - \beta} \cdot \frac{a_{\rm SF}|_{\varepsilon_* = 0}}{\sqrt{a_0a_b}}\right), \quad (B.6)$$

where we treated ε_* as a constant that we can pull out of $a_{\rm SF}$ (see Appendix A.1). Thus, at fixed a_b , the total acceleration $a_{\rm tot}$ decreases as a function of large ε_* as long as

$$\varepsilon_* < \frac{\sqrt{a_0 a_b}}{a_{\rm SF}|_{\varepsilon_*=0}} \cdot \frac{3-\beta}{2\beta-3} \simeq \frac{r_c^2}{r_{\rm MOND} \cdot r} \cdot \frac{3-\beta}{2\beta-3} = \frac{6}{2\beta-3} \frac{M_{\rm Pl}}{r} \frac{\alpha}{m^2}, \tag{B.7}$$

with the MOND radius $r_{\text{MOND}} = \sqrt{GM_b/a_0}$ and r_c as defined in Appendix A.1.1. Numerically, for the fiducial parameter values from Berezhiani et al. (2018),

$$\varepsilon_* \lesssim 107 \cdot \left(\frac{5 \,\mathrm{kpc}}{r}\right).$$
 (B.8)

Thus, the total acceleration is a decreasing function of ε_* for a significant range of large ε_* values so that going to large ε_* is one way to allow for relatively large baryonic masses.

Appendix C: Method

C.1. Data

As already mentioned in Sect. 3, we used the observed rotation velocity $V_{\rm obs}$ directly from SPARC. We did not allow distance or inclination as a fit parameter, so we did not vary $V_{\rm obs}$ in our fitting procedure. As also described in Sect. 3, we obtained the baryonic energy density $\rho_b(R,z)$ from the surface densities provided by SPARC,

$$\rho_b(R, z) = \rho_{\text{gas}}(R, z) + 0.5 \cdot Q_* \cdot \rho_*(R, z) + 0.7 \cdot Q_* \cdot \rho_{\text{bulge}}(\sqrt{R^2 + z^2}).$$
 (C.1)

The fit parameter Q_* parametrizes the stellar mass-to-light ratio. For later use, we numerically solved the Poisson equation

$$\Delta\left(-\frac{\hat{\mu}_x}{m}\right) = 4\pi G \rho_x,\tag{C.2}$$

separately for $\rho_x \in \{\rho_{\rm gas}, \rho_*, \rho_{\rm bulge}\}$ using the Mathematica code used in Hossenfelder & Mistele (2020). This allows us to quickly get a solution to the Poisson equation sourced by the full ρ_b with arbitrary Q_* by the rescaling

$$\frac{\hat{\mu}_b}{m} = \frac{\hat{\mu}_{\text{gas}}}{m} + 0.5 \cdot Q_* \cdot \frac{\hat{\mu}_*}{m} + 0.7 \cdot Q_* \cdot \frac{\hat{\mu}_{\text{bulge}}}{m},$$
 (C.3)

where the quantity $\hat{\mu}_b/m$ is minus the standard Newtonian gravitational potential up to an additive constant (see also the next subsection). The numerical procedure solves the Poisson equation within a sphere with radius r_{∞} assuming a $z \rightarrow -z$ symmetry. We assumed spherically symmetric boundary conditions for $\hat{\mu}_b$. Specifically,

$$\frac{\hat{\mu}_x}{m}\bigg|_{\sqrt{R^2 + z^2} = r_{\infty}} = 0. \tag{C.4}$$

This is reasonable for sufficiently large r_{∞} . We used $r_{\infty}=100\,\mathrm{kpc}$ except when the SPARC V_{obs} data extend to radii larger than $100\,\mathrm{kpc}$. Then, we increased r_{∞} in steps of 5 kpc until r_{∞} was larger than the maximum radius of the V_{obs} data points.

C.2. SFDM calculation

We assume that each galaxy's $V_{\rm obs}$ data points lie within its superfluid core. This is discussed in more detail in Appendix D.2.7. Then, in SFDM, there are two equations for a galaxy in equilibrium inside the superfluid core. One for the phonon acceleration, a_{θ} , and one for the quantity $\hat{\mu}$, which contains the Newtonian gravitational potential (see Appendix A.1).

Even in a fully axisymmetric calculation, one can impose spherically symmetric boundary conditions for the fields $\hat{\mu}$ and θ at some large radius r_{∞} (Hossenfelder & Mistele 2020). The value of θ at r_{∞} is inconsequential, so one can choose $\theta(r_{\infty})=0$. For $\hat{\mu}$, its value μ_{∞} at r_{∞} is important. It determines the size of the superfluid halo and is a free parameter in the boundary conditions. We used a parameter similar to μ_{∞} as a free fit parameter in our fitting procedure.

It is useful to split $\hat{\mu}$ into a part called $\hat{\mu}_b$ sourced only by ρ_b and the rest called $\hat{\mu}_{SF}$. That is, $\hat{\mu} = \hat{\mu}_b + \hat{\mu}_{SF}$ with

$$\Delta\left(-\frac{\hat{\mu}_b}{m}\right) = 4\pi G \rho_b \,, \tag{C.5}$$

$$\Delta \left(-\frac{\hat{\mu}_{SF}}{m} \right) = 4\pi G \rho_{SF} \left[\hat{\mu}_b + \hat{\mu}_{SF}, \nabla \theta \right]. \tag{C.6}$$

We used boundary conditions $\hat{\mu}_b(r_\infty) = 0$ and $\hat{\mu}_{SF}(r_\infty) = \mu_\infty$. We calculated $\hat{\mu}_b$ as described in the previous subsection.

C.2.1. A simple approximation

For our fits, we did not do a fully axisymmetric calculation. Instead, we used an approximation that is much faster to compute. Our approximation mainly consists of using a no-curl approximation for a_{θ} and assuming spherical symmetry for $\hat{\mu}_{SF}$. As discussed in Appendix A.1, the no-curl approximation means that we get a_{θ} as an algebraic function of a_{b} and $\hat{\mu}$.

The second part of our approximation is assuming spherical symmetry for $\hat{\mu}_{SF}$ in $\hat{\mu} = \hat{\mu}_b + \hat{\mu}_{SF}$. That is, the part of $\hat{\mu}$ due to the superfluid's self-gravity is spherically symmetric. Only the baryonic part produces an axisymmetric $\hat{\mu}$. This is a reasonable approximation for the following reason. A fully axisymmetric calculation gives a $\hat{\mu}$ that is not spherically symmetric only at relatively small radii. At these radii, $\hat{\mu}_b$ dominates. At larger radii, even a fully axisymmetric calculation gives a spherically symmetric $\hat{\mu}$ (Hossenfelder & Mistele 2020). Indeed, we imposed spherically symmetric boundary conditions at larger radii. Only at these larger radii does $\hat{\mu}_{SF}$ usually become important.

We calculated $\hat{\mu}_{SF}(r)$ from Eq. (C.6), which contains the function $\hat{\mu}_b(R,z)$. To solve this equation in spherical symmetry, we need to make a choice of which R and z to use in evaluating $\hat{\mu}_b(R,z)$ for each r. The same applies to $a_b(R,z)$, which enters indirectly through a_θ . We chose R=r and z=0. Different choices may give slightly different results.

For ρ_{SF} , we used the expression Eq. (A.8) valid in the no-curl approximation. The function $f_{\beta}(\varepsilon_*)$ in this expression for ρ_{SF} is known analytically but is relatively slow to evaluate numerically. To speed up the calculation, for a given β , we evaluated f_{β} as a function of $\log_{10}(\varepsilon_* - \varepsilon_{*\min})$ on an evenly spaced grid with grid spacing 0.01 and linearly interpolated between the grid points. We used the resulting linear interpolation in our calculation since it is faster to evaluate numerically than the analytical form of f_{β} .

Below, we refer to this approximation as the "simple" approximation. In Appendix C.2.3, we explicitly demonstrate that it works well using a few example galaxies.

C.2.2. Calculation using the "simple" approximation

We calculated $\hat{\mu}_b$ as described above in Appendix C.1. From this, we got a_b as $-\nabla \hat{\mu}_b/m$. In accordance with our simple approximation, we used the no-curl approximation for a_θ so that we got a_θ as an algebraic function of a_b and $\hat{\mu}_b + \hat{\mu}_{SF}$ (see Appendix A.1). The remaining part was to calculate $\hat{\mu}_{SF}$. This then also gave a_{SF} as $-\nabla \hat{\mu}_{SF}/m$.

For $\hat{\mu}_{SF}$ we assumed spherical symmetry and we used the form Eq. (A.8) for ρ_{SF} valid in the no-curl approximation. Then, Eq. (C.6) becomes

$$\frac{1}{r^2} \partial_r \left(r^2 \partial_r \left(-\frac{\hat{\mu}_{\rm SF}(r)}{m} \right) \right) = 4\pi G \rho_{\rm SF} \left(\varepsilon_*, |\boldsymbol{a}_b| \right), \tag{C.7}$$

where

$$\varepsilon_* = \frac{2m^2}{\alpha M_{\rm Pl} |\mathbf{a}_b|} \frac{\hat{\mu}_b + \hat{\mu}_{\rm SF}}{m}.\tag{C.8}$$

The non-spherically symmetric functions $a_b(R, z)$ and $\hat{\mu}_b(R, z)$ are evaluated at R = r, z = 0.

This is a second-order ODE for $\hat{\mu}_{SF}$. As boundary conditions we chose

$$\hat{\mu}'_{SE}(dr) = 0, \tag{C.9}$$

$$\hat{\mu}_{\rm SF}(R_{\rm mid}) + \hat{\mu}_b(R_{\rm mid}, 0) = \varepsilon \frac{\alpha M_{\rm Pl} |\boldsymbol{a}_b(R_{\rm mid}, 0)|}{2m} \,. \tag{C.10}$$

With dr=0, the first boundary condition is a standard regularity condition at the origin. To avoid numerical issues, we chose a small nonzero value for dr, usually $dr=10^{-8}$ kpc. The second condition corresponds to a choice of $\varepsilon=\varepsilon_*(R_{\rm mid})$ (see Eq. (1)). It parametrizes how close to the MOND limit $|\varepsilon_*|\ll 1$ a galaxy is in the middle of the $V_{\rm obs}$ data points.

Solutions for $\hat{\mu}$ are such that they typically reach their minimum allowed value $\hat{\mu}_{\min}$ (see Eq. (A.13)) at some finite radius. Beyond this radius, assuming a superfluid core makes no sense. Thus, whenever solutions ended up with $\hat{\mu} < \hat{\mu}_{\min}$ at some radius $dr \le r \le R_{\max}$, we discarded them, since we assumed all data points lie within the superfluid core.

Sometimes, Mathematica fails to solve the equations for numerical reasons. This is indicated by its "NDSolve" producing a "FindRoot::sszero," a "NDSolveValue::berr," or a "NDSolveValue::evcvmit" error that we can check for. In this case, we automatically decreased dr by factor of 100 and retried.

C.2.3. Validating the simple approximation

Here, we explicitly compare the simple approximation described in Appendix C.2.1 against a fully axisymmetric calculation. For definiteness, we used the best-fit Q_* and f_{ε_*} values for SFDM (see Appendix C.3).

For the fully axisymmetric calculation we used the Mathematica code from Hossenfelder & Mistele (2020). This code expects boundary conditions in the form $\hat{\mu}(r_{\infty}) = \mu_{\infty}$ for some r_{∞} and μ_{∞} . We chose $r_{\infty} = 100\,\mathrm{kpc}$ unless stated otherwise. Our simple approximation instead uses a value of $\hat{\mu}_{\mathrm{SF}}(R_{\mathrm{mid}})$ as a boundary condition. To compare our simple calculation and the fully axisymmetric calculation for the same physical boundary conditions, we first did the simple calculation with the best-fit values for Q_* and f_{ε_*} . We then evaluated the solution $\hat{\mu}$ from this simple calculation at $r = r_{\infty}$ and used the resulting value as the boundary condition μ_{∞} for the fully axisymmetric calculation.

Our simple calculation makes two main approximations. First, we used the no-curl approximation for the phonon force.

Second, we assumed spherical symmetry for $\hat{\mu}_{SF}$. When our simple calculation disagrees with the fully axisymmetric calculation we want to know which of these two parts is responsible for the deviation. To this end, we did a third calculation where we used the fully axisymmetric calculation for $\hat{\mu}$, but then used the nocurl approximation when calculating a_{θ} for the rotation curve. We refer to this as the "full+nocurl" calculation.

In Fig. C.1, left, we show the rotation curve and $\hat{\mu}/m$ for NGC 2403 for the different types of calculation described above. The calculations differ by a few percent at intermediate radii. The full+nocurl rotation curve lies pretty much on top of the simple rotation curve, while the "full" rotation curve differs from the two others at intermediate radii. Thus, the no-curl approximation is the source of the this difference between the full and the simple calculations. For $\hat{\mu}$, all calculations agree almost perfectly with each other (see Fig. C.1, right).

This same qualitative result holds for DDO 064 shown in Fig. C.2. This is an example of a galaxy that is in the proper MOND limit $|\varepsilon_*| \ll 1$ almost everywhere at $R_{\min} \leq R \leq R_{\max}$. The no-curl approximation does not always lead to visible deviations between the full and the simple calculations. An example is IC 2574 where the full and simple calculations agree almost perfectly with each other (see Fig. C.3).

Thus, our simple approximation works well, with the main error being due to the no-curl approximation.

C.3. Fitting method

For SFDM, we used the two parameters

$$f_Y \equiv \log_{10}(Q_*),\tag{C.11}$$

for the stellar mass-to-light ratio (see Eq. (C.1)), and

$$f_{\varepsilon_*} \equiv \log_{10} \left(\varepsilon - \varepsilon_{*\min} \right),$$
 (C.12)

for the superfluid halo (see Eq. (C.12)), as fit parameters. Here, $\varepsilon_{*\min}$ is the minimum possible value of ε_{*} where ρ_{SF} vanishes (see Eq. (A.12)). We did not vary the model parameters m, α , Λ , and β . We used Mathematica's "NMinimize" with the "Nelder-Mead" method to find the smallest χ^{2} for each galaxy,

$$\chi^2 = \frac{1}{N - f} \sum_{R} \frac{(V_{\text{obs}}(R) - V_c(R))^2}{\sigma_{V_{\text{obs}}}^2(R)}.$$
 (C.13)

Here, N is the number of data points in the galaxy, f=2 is the number of fit parameters, $\sigma_{V_{\rm obs}}$ is the uncertainty on the velocity $V_{\rm obs}$ from SPARC, $V_c(R)$ is the calculated rotation curve in SFDM, and the sum is over the data points at radii R.

We minimized χ^2 for f_Y and f_{ε_*} in the range Eqs. (7) and (8). When f_{ε_*} is too small, it can happen that $\hat{\mu}$ does not exist with the desired parameters, as discussed in Appendix C.2.2. In this case, we artificially set $\chi^2 = 10^{10}$. Then, NMinimize continued searching elsewhere.

The NelderMead search method is faster than a simple grid search but can get stuck in local minima. To avoid this, we ran NMinimize three times with different starting points. Of the three results, we used that with the smallest χ^2 . The first run is with the "RandomSeed" option set to 0, the second with the RandomSeed option set to 1, and the third run is with the starting points (0,0), (-0.5,0), and (0,-0.5). The third run is to guarantee that the point $f_Y = 0$ is visited at least once, since this point corresponds to the M/L_* expected from SPS models.

To further reduce the needed computation time we rounded f_Y and f_{ε_*} to 0.01 before any calculation. For (un-rounded) f_Y

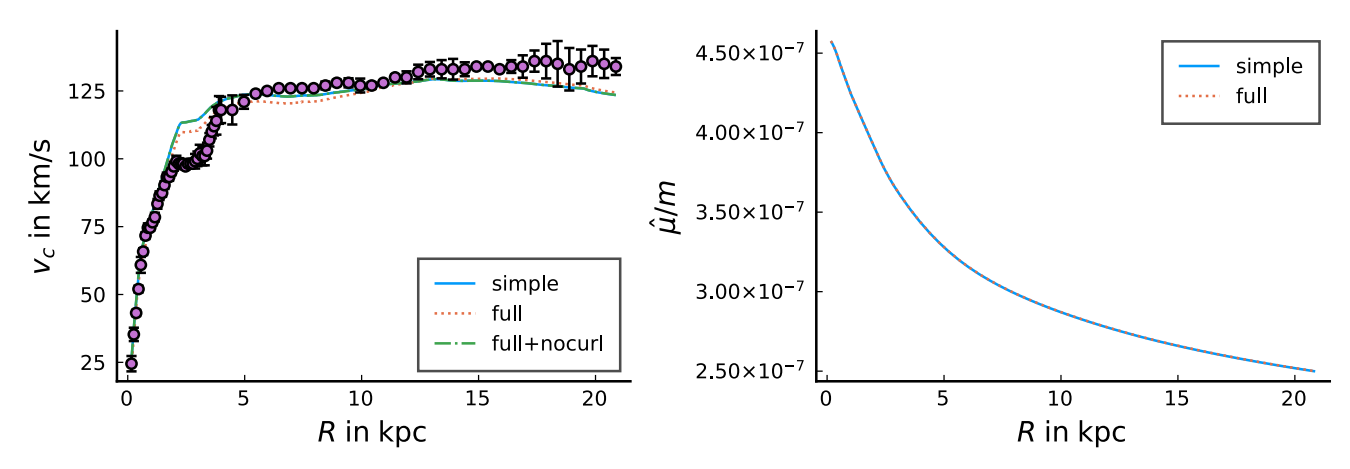


Fig. C.1. Results of different types of calculations in SFDM for NGC 2403. The simple calculation is the approximation described in Appendix C.2.1. The full calculation is the fully axisymmetric SFDM calculation. The full+nocurl calculation uses the same $\hat{\mu}(R,z)/m$ as the full calculation but uses a no-curl approximation for the phonon acceleration, a_{θ} . This is for the best-fit parameters obtained in Appendix D.2. Left: Rotation curve for the different types of calculations (lines) and the observed rotation curve from the SPARC data (circles with error bars). Right: Field $\hat{\mu}/m$ for the same types of calculations, except for full+nocurl, which has the same $\hat{\mu}/m$ as the full calculation.

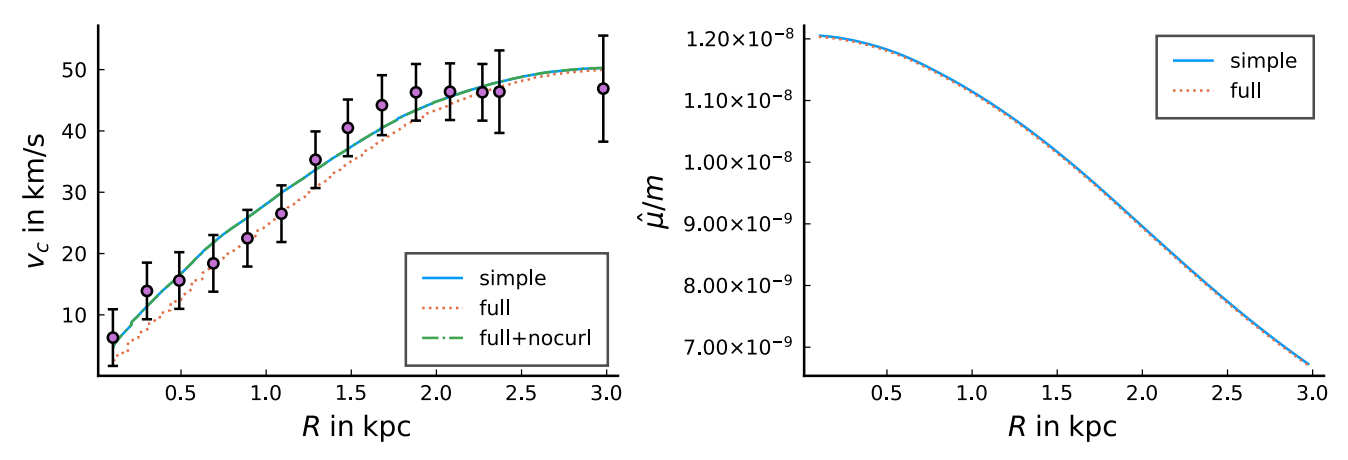


Fig. C.2. Same as Fig. C.1 but for DDO 064. This is an example of a galaxy in the MOND limit $|\varepsilon_*| \ll 1$.

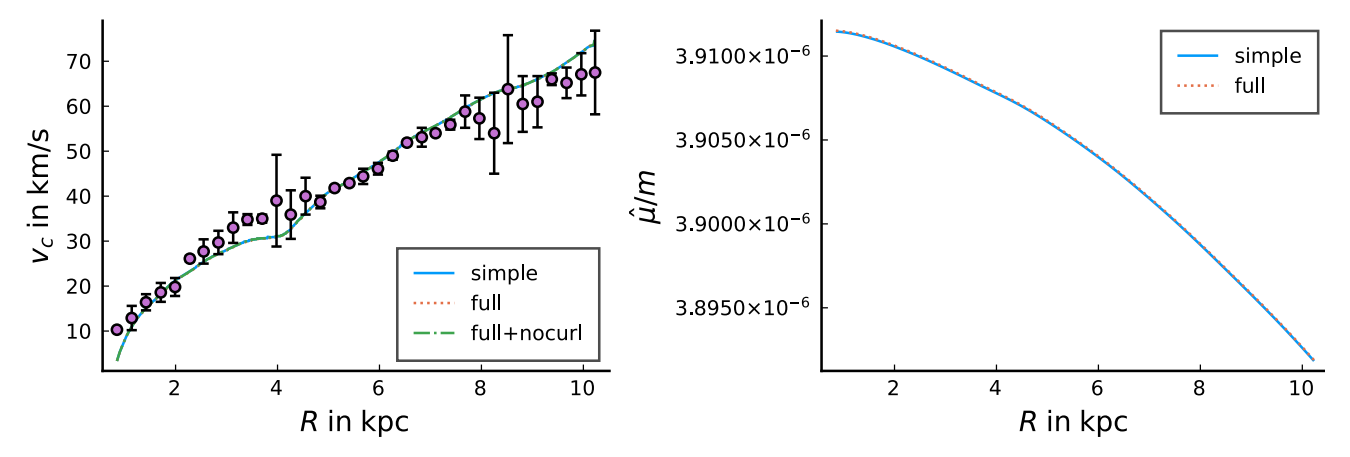


Fig. C.3. Same as Fig. C.1 but for IC 2574.

and f_{ε_*} that give the same rounded values as a previous calculation, we reused the previous results without a new computation.

This fitting method is much simpler than the MCMC method used in Li et al. (2018). Still, as we will see in Appendix D.1, we found similar results for the stellar M/L_* as Li et al. (2018) for a standard MOND model. In addition, for SFDM we could not set up informative priors on f_{ε_*} anyway since

there is so far no cosmology from which to infer such a prior.

In the SPARC data, the Newtonian acceleration due to gas sometimes points outward from the galactic center, not toward it. Usually, such a negative gas contribution is countered by the positive contributions from the stellar disk and bulge such that the total a_b points to the galactic center. But sometimes this is not

the case, especially for small f_Y . When this happened, we simply ignored the data points where a_b is negative when calculating χ^2 .

As a cross-check and as a comparison for SFDM, we also fitted the RAR to the SPARC data, that is, we fitted the SPARC data with MOND assuming no curl term and the exponential interpolation function v_e (Lelli et al. 2017b). We call this the "MOND" model. In this case, we have only one free fit parameter, f_Y . Thus, when calculating χ^2 , we set f=1. Also, we used the "SimulatedAnnealing" method of Mathematica's NMinimize function with one run instead of the NelderMead method with three runs. We did not round f_Y to 0.01 for these MOND fits.

Below we consider modifications of both the SFDM model and the MOND model. The SFDM-based models will be fitted as the "SFDM" model. The MOND-based models will be fitted as the MOND model. We will discuss the details of these modifications below.

For the SFDM models, we parametrize the total dark matter within the last rotation curve data point R_{max} by a parameter, $f_{M_{\text{DM}}}$,

$$f_{M_{\rm DM}} \equiv \log_{10} \left(\frac{M_{\rm DM}(R_{\rm max})}{M_{\rm DM}^{MP}(R_{\rm max})} \right), \tag{C.14}$$

where $M_{\rm DM}^{MP}(R)$ is defined by

$$\sqrt{a_0^{\text{SFDM}} a_b(R, z=0)} + a_{\text{SF}}(R, z=0) \equiv \sqrt{a_0^{\text{RAR}} a_b(R, z=0)},$$
(C.15)

with $a_{\rm SF} \equiv GM_{\rm DM}^{MP}/R^2$ and with the SPS M/L_* values for a_b (i.e. $M/L_*=0.5$ for the disk and $M/L_*=0.7$ for the bulge). The parameter $f_{M_{\rm DM}}$ measures how far the dark matter mass at $R_{\rm max}$ is away from the reference value $M_{\rm DM}^{MP}$. This reference value $M_{\rm DM}^{MP}$ is defined such that the associated dark matter acceleration $a_{\rm SF}$ counters the difference in $\sqrt{a_0a_b}$ between MOND and SFDM due to the different choice for a_0 (see Appendix B.1). Thus, $f_{M_{\rm DM}}$ parametrizes how large the dark matter mass is relative to the mass that cancels this a_0 difference.

C.4. Two-field SFDM calculation

We can use the same calculation and fitting procedure as for standard SFDM. We simply have to adjust the expression for the superfluid energy density and the algebraic no-curl solution of the phonon force. Apart from that, we adjusted the calculation only in two ways that we now explain.

The superfluid energy density, $\rho_{\rm SF}$, of two-field SFDM is linear in $\hat{\mu}/m$ and depends on no other fields. This allows the calculation to be sped up. For a given galaxy, we first calculated one particular solution, $\hat{\mu}_{\rm SF}$, of the full, inhomogeneous equation as previously described,

$$\Delta\left(-\frac{\hat{\mu}_{\rm SF}}{m}\right) = \frac{1}{r_0^2} \frac{\hat{\mu}_b + \hat{\mu}_{\rm SF}}{m}.\tag{C.16}$$

To get solutions for the same galaxy with different boundary conditions, we can add solutions of the homogeneous equation to the so-obtained $\hat{\mu}_{SF}$. Since we assume spherical symmetry, the solutions to the homogeneous equation are $A \sin(r/r_0)/r$ for arbitrary A. To get a solution for some desired boundary condition, we just needed to choose an appropriate A.

For standard SFDM, we used $\varepsilon_*(R_{\rm mid})$ in the range $\varepsilon_{*{\rm min}}$ + 10^{-2} to $\varepsilon_{*{\rm min}}$ + 10^4 as the boundary condition for $\hat{\mu}$. For two-field SFDM, we must adjust this range. This is because, in two-field

SFDM, the phonon force can more easily reach the MOND limit $|\varepsilon_*| \ll 1$ (i.e., typical values of $|\varepsilon_*|$ are much smaller). Thus, we changed the range of $\varepsilon_*(R_{\rm mid})$ values scanned by our fit code to be

$$10^{-6} \le \varepsilon_*(R_{\text{mid}}) \le 1. \tag{C.17}$$

We note that $\varepsilon_{*\min} = 0$ in two-field SFDM. We will later see that no galaxies end up at the boundaries of this range, so it seems to be reasonable.

Appendix D: Results

D.1. M/L_* in MOND

Our MOND fit should give results roughly comparable to Li et al. (2018), which also fitted the RAR to SPARC galaxies. A difference is that Li et al. (2018) used an MCMC procedure with Gaussian priors, while we used a simple parameter scan to minimize χ^2 . We also did not vary distance and inclination and did not separately vary the mass-to-light ratio of the stellar disk and the bulge. As a consequence of this simplified fitting procedure, the distribution of best-fit M/L_* has more outliers and looks less like a Gaussian in our case compared to Li et al. (2018). This can be seen for example in Fig. D.2, which shows the histograms for the best-fit f_Y for the galaxies with the SPARC quality flag q = 1.

Still, the median best-fit stellar mass-to-light ratios and the best-fit χ^2 values are similar to those from Li et al. (2018). The median stellar disk M/L is 0.39. When we restrict the ourselves to q=1 galaxies, this becomes 0.47. This is shown in Table D.1. This is in reasonable agreement with Li et al. (2018), who obtained 0.50. We show the cumulative χ^2 distribution in Fig. D.1, which is also in reasonable agreement with Li et al. (2018).

In Fig. D.2, one sees that some galaxies end up at the minimum stellar mass-to-light ratio allowed in our fitting method, corresponding to $Q_* \approx 0.01$. If we do not restrict ourselves to q = 1, this peak at $Q_* \approx 0.01$ is even more pronounced. These galaxies with $Q_* \approx 0.01$ come about as follows. Consider a galaxy where the observed $V_{\rm obs}$ is smaller than that computed in MOND. The computed rotation curve can be brought closer to $V_{\rm obs}$ by decreasing M/L_* . It can happen that M/L_* must be reduced so much that the gas component, which is unaffected by M/L_* , dominates. When this happens and when $V_{\rm obs}$ is still smaller than the computed rotation velocity, the fitting code will continue to decrease M/L_* to improve χ^2 . But of course this will only barely change χ^2 since the gas component dominates, and the galaxy ends up at the minimum allowed mass-to-light ratio corresponding to $Q_* = 0.01$. This does not happen in Li et al. (2018), since varying the distance and inclination can avoid such situations and also because the Gaussian priors discourage going to the minimum allowed M/L_* .

Thus, the best-fit mass-to-light ratios of the galaxies at $Q_* = 0.01$ should not be taken seriously. They are an artifact of our simplified fitting procedure. They have a comparably good fit also with larger Q_* . We verified that the galaxies at $Q_* = 0.01$ are gas-dominated at their best-fit Q_* . To check that our results do not depend on these outlier galaxies, we also include a column in Table D.1 that averages only over the galaxies where the MOND fit gives $\log_{10} Q_* > -1.5$. This gives a median stellar disk M/L of 0.44. This lies between the result for the q=1 galaxies and the one we got when not restricting the galaxies.

In Table D.1 and Fig. D.1, we also show the results for a fourth quality cut we call "thermal ok." This refers to the galaxies where, in our SFDM fit discussed below, a simple estimate

Table D.1. Median $0.5 \times Q_*$ for the best fit for different models and galaxy cuts.

Name	all	q = 1	MOND $\log_{10} Q_* > -1.5$	thermal ok
MOND	0.394	0.469	0.443	0.395
MOND $\nu_{ heta}$	$\times 0.74$	$\times 0.74$	×0.75	×0.73
MOND $v_{\theta} + a_0^{\text{SFDM}}$	$\times 0.97$	$\times 0.89$	×0.93	×0.97
SFDM	$\times 1.18$	$\times 1.04$	×1.10	×1.25
SFDM $a_{\theta} = \sqrt{a_0 a_b}$	$\times 0.92$	$\times 0.87$	×0.88	×0.92
SFDM $\beta = 1.55$	$\times 0.90$	$\times 0.87$	×0.90	×0.91
SFDM $ \varepsilon < 5$	$\times 0.96$	$\times 0.89$	×0.92	×0.96
SFDM $ \varepsilon < 0.4$	$\times 0.96$	$\times 0.90$	×0.94	×0.95
SFDM $ \varepsilon $ < 0.4 (no bad fits)	$\times 0.94$	$\times 0.89$	×0.92	×0.94
two-field	$\times 0.90$	$\times 0.87$	×0.88	×0.91
two-field a_{\min}^{small}	$\times 0.90$	$\times 0.87$	×0.88	×0.91
two-field $a_b > a_{\min}^{\text{small}}$	×0.90	×0.87	×0.88	×0.91

Notes. Each row corresponds to a different model, and each column corresponds to a different cut on the included galaxies. The first row shows the values for the MOND fits, and the other rows show the factor relative to the MOND fits.

Table D.2. Same as Table D.1 but for the mean instead of the median $0.5 \times Q_*$.

Name	all	<i>q</i> = 1	MOND $\log_{10} Q_* > -1.5$	thermal ok
MOND	0.534	0.614	0.613	0.558
MOND $\nu_{ heta}$	$\times 0.74$	$\times 0.75$	×0.74	×0.74
MOND $v_{\theta} + a_0^{\text{SFDM}}$	$\times 0.96$	$\times 0.96$	×0.96	×0.96
SFDM	$\times 1.46$	$\times 1.29$	×1.32	×1.55
SFDM $a_{\theta} = \sqrt{a_0 a_b}$	$\times 0.85$	$\times 0.87$	×0.85	×0.84
SFDM $\beta = 1.55$	$\times 0.87$	$\times 0.84$	×0.84	×0.86
SFDM $ \varepsilon < 5$	$\times 0.93$	$\times 0.92$	×0.93	×0.93
SFDM $ \varepsilon < 0.4$	$\times 1.07$	$\times 1.14$	×1.07	×0.97
SFDM $ \varepsilon $ < 0.4 (no bad fits)	$\times 0.95$	$\times 0.96$	×0.95	×0.94
two-field	$\times 0.84$	$\times 0.88$	×0.84	×0.82
two-field a_{\min}^{small}	$\times 0.84$	$\times 0.88$	×0.84	×0.82
two-field $a_b > a_{\min}^{\text{small}}$	×0.83	×0.87	×0.83	×0.81

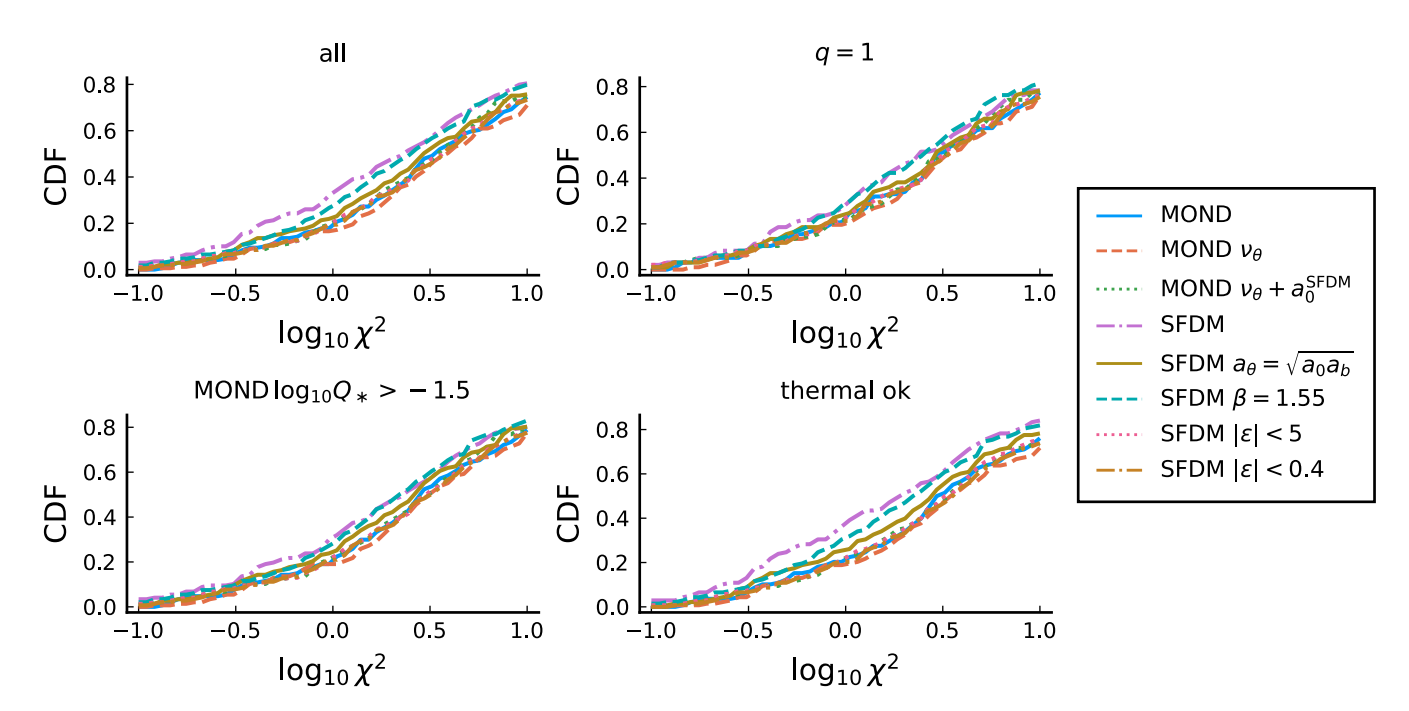


Fig. D.1. χ^2 CDFs for the different MOND and SFDM models and for different galaxy cuts.

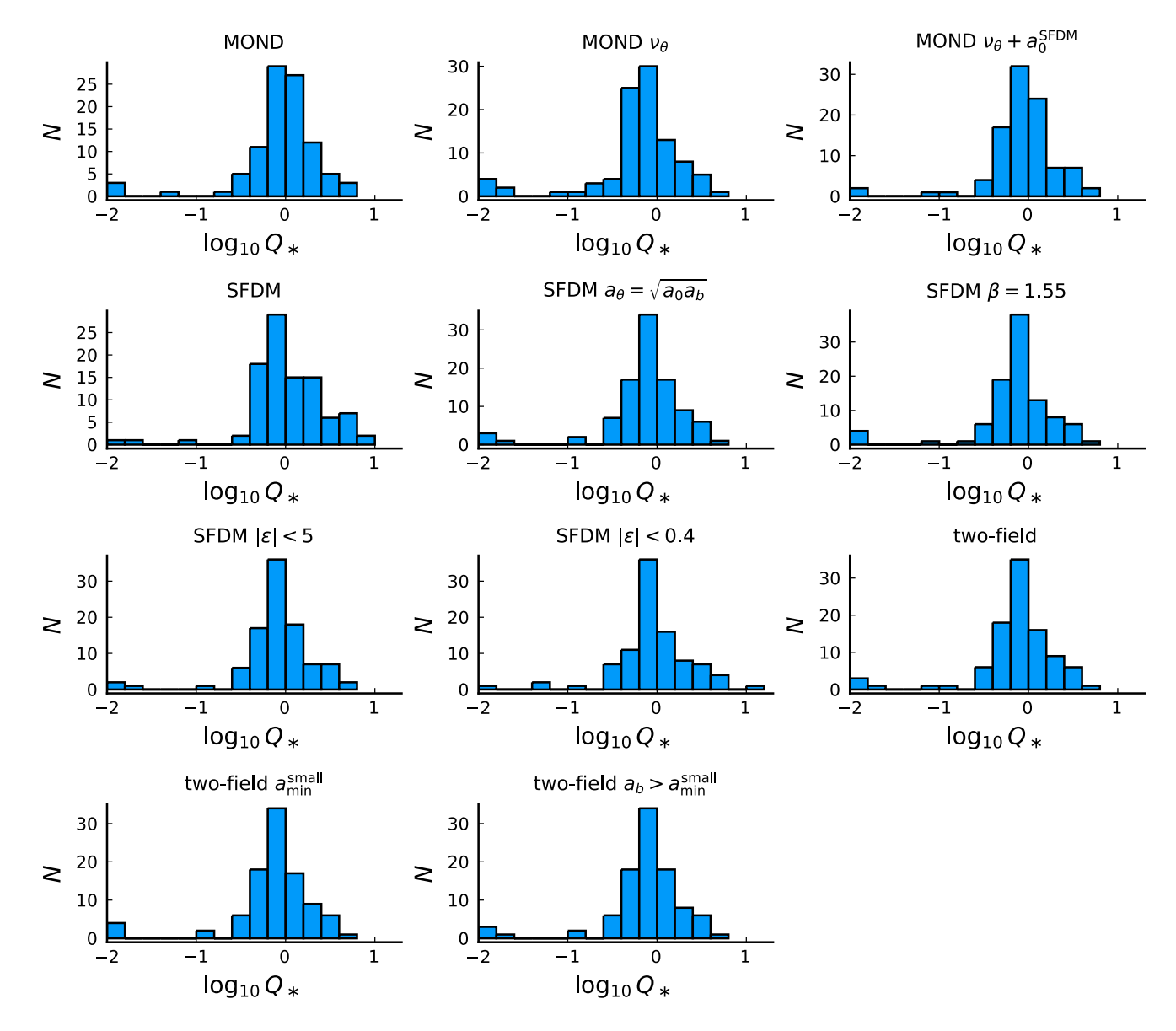


Fig. D.2. Histograms of the best-fit f_Y values for the different models restricted to the q=1 galaxies.

shows that all SPARC data points lie within the superfluid core of the galaxy (see Appendix D.2.7 for more details). Here, we just note that this quality cut does not qualitatively change our results.

We show the mean stellar disk mass-to-light ratios in Table D.2. These differ from the median values for all quality cuts because the resulting f_Y distributions are not Gaussian as already discussed.

D.2. M/L_* in SFDM

For SFDM, we show the χ^2 CDF in Fig. D.1 and the Q_* and $f_{M_{\rm DM}}$ histograms for the q=1 galaxies in Fig. D.2 and Fig. D.3. The χ^2 CDF and the Q_* histogram look qualitatively similar to those from the MOND fit, just with some numerical differences. For example, as for the MOND fit, there are some galaxies at the minimum value $Q_*=0.01$. These are the galaxies that become gas-dominated during the fitting procedure as explained in Appendix D.1. The precise distribution of best-fit $f_{M_{\rm DM}}$ values should not be taken too seriously, especially at smaller values.

This is because the superfluid halo's Newtonian gravitational pull is often subdominant in SFDM, so that our fitting method cannot really distinguish different $f_{M_{\rm DM}}$ values, as long as $a_{\rm SF}$ stays subdominant.

D.2.1. Stellar mass-to-light ratio

Our initial question was whether or not SFDM needs a smaller M/L_* than standard MOND models. We find that this is not necessarily the case. In SFDM, the median stellar disk M/L is 0.49 for the q=1 galaxies. This is not much smaller than MOND. The numerical details depend on whether one considers the mean or the median and on the chosen galaxy cuts (see Tables D.1 and D.2). Still, a robust finding across all of these choices is that SFDM does not give a significantly smaller Q_* than MOND.

There are two reasons for this. First, contrary to what one would hope for in SFDM, many galaxies do not end up in the MOND limit $|\varepsilon_*| \ll 1$. If the phonon force a_θ is close to its MOND-limit value $\sqrt{a_0 a_b}$, SFDM does give smaller averaged Q_* than MOND. Second, even in the MOND limit, the best-fit

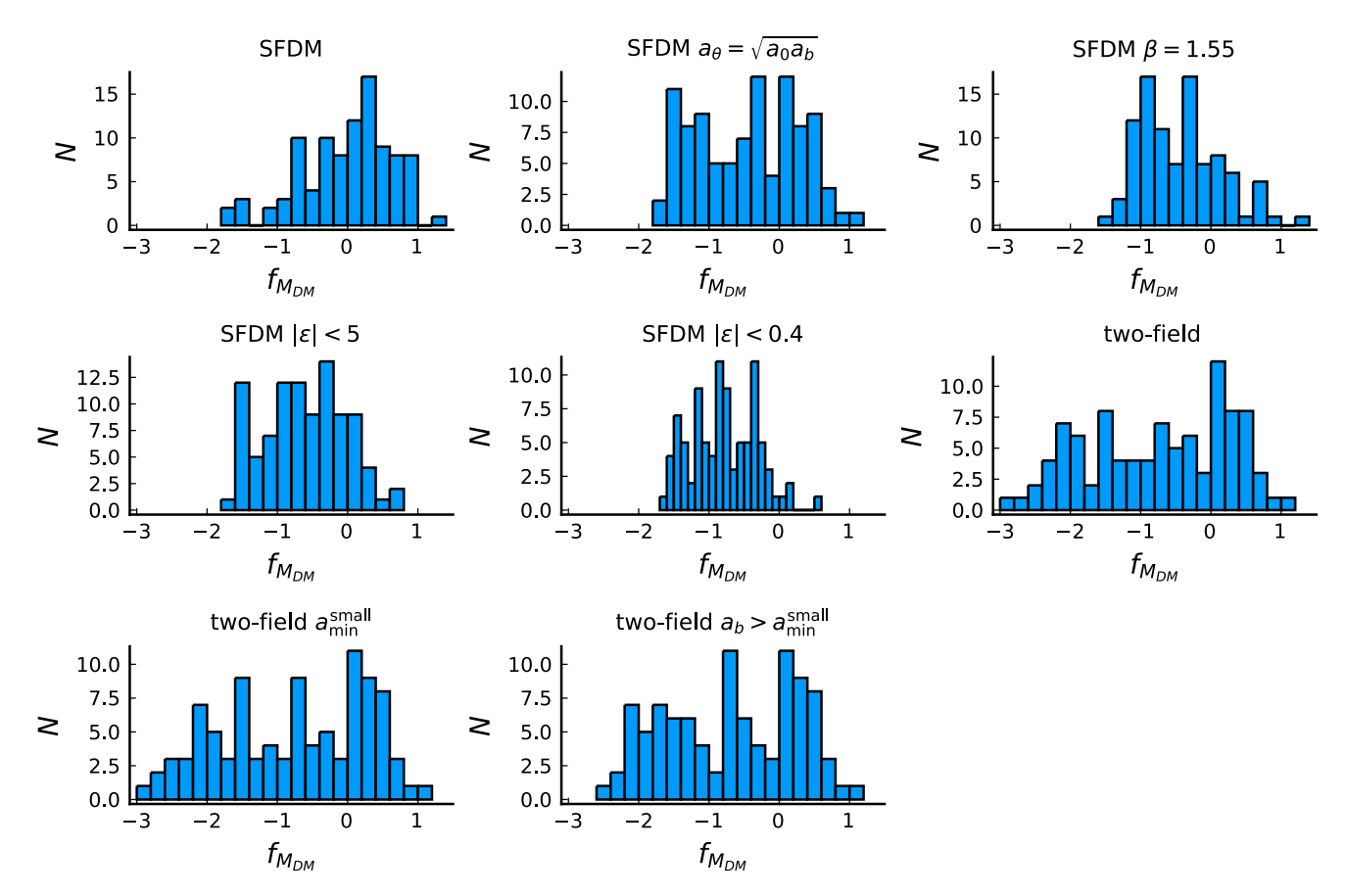


Fig. D.3. Histograms of the best-fit $f_{M_{DM}}$ values for the different models restricted to the q=1 galaxies.

 Q_* values in SFDM are systematically smaller than in MOND only for certain galaxy types. Such trends are not expected from SPS models. It also means we can never say that SFDM universally requires a smaller or larger Q_* than MOND. We can make such statements only for a given galaxy sample. We now discuss these two points in more detail.

D.2.2. Effect of going outside the MOND limit on M/L_*

As discussed in Appendix B.2, going to $\varepsilon_* \gg 1$ allows us to make a_θ smaller so that a larger M/L_* is possible. This could be one reason why the averaged M/L_* is relatively large in SFDM.

As a first check, we show a scatter plot of Q_* versus $\varepsilon_*(R_{\rm mid})$ (see Fig. 3). Indeed, many galaxies have $\varepsilon_*\gg 1$. In addition, Fig. 3 shows a correlation between ε_* and Q_* . Galaxies with $\varepsilon_*\gg 1$ tend to have a larger Q_* . This fits with the idea that we do not find a smaller M/L_* for SFDM because many galaxies are not in the MOND limit.

To confirm this, we redid the SFDM fit, but with the phonon acceleration a_{θ} replaced by its MOND limit value $\sqrt{a_0a_b}$ when calculating rotation curves. The calculation of $\hat{\mu}$ was left untouched. This is the model shown as "SFDM $a_{\theta} = \sqrt{a_0a_b}$ " in, for example, Table D.1 and Fig. D.2. With this model, the trick of going to $\varepsilon_* \gg 1$ to make the phonon acceleration a_{θ} small does not work. Indeed, the averaged M/L_* is now significantly smaller than for the original SFDM fit. This result is again robust against different choices for the galaxies we consider and different choices for the averaging function. We can also see explicitly in Fig. D.4 that the distribution of best-fit ε values has migrated to smaller values compared to the original SFDM fit.

As a third check, we redid the SFDM fit, but with the model parameter β set to 1.55 instead of 2. This choice makes it much harder to make the phonon acceleration a_{θ} small by going to large $\varepsilon_* \gg 1$, as can be seen from Fig. A.1. This is the model shown as "SFDM $\beta=1.55$ " in, for example, Table D.1 and Fig. D.2. If our explanation for the large M/L_* in SFDM is correct, this modified model should again have significantly smaller M/L_* . Indeed, this SFDM $\beta=1.55$ model gives results that are comparable to those from the SFDM $a_{\theta}=\sqrt{a_0a_b}$ model. That is, M/L_* is now significantly smaller than for the SFDM fit. Similarly, the resulting ε values are much smaller than in the original SFDM fit (see Fig. D.4).

Thus, one reason for the relatively large M/L_* in SFDM is indeed that many galaxies are not actually in the MOND limit.

D.2.3. Enforcing the MOND limit

Its MOND limit is one of the main motivations of SFDM, because then rotation curves are automatically MOND-like. This is not the case outside the MOND limit (i.e., when ε_* is not small). Then MOND-like rotation curves are not possible without adjusting the boundary condition separately for each galaxy. Thus, our fit results for SFDM go against the original motivation behind SFDM.

We may wonder if large ε_* values are really necessary for SFDM to get reasonable fits of the SPARC data. It is possible that our fit code went to $\varepsilon_*\gg 1$ for little gain in χ^2 . To check this, we redid the SFDM fit, but with $\varepsilon=\varepsilon_*(R_{\rm mid})$ restricted to $|\varepsilon|<0.1$. Whenever we solved the SFDM equations and found $|\varepsilon|\geq0.1$, we manually set $\chi^2=10^7(1+|\varepsilon|)$ so that the fitting code went

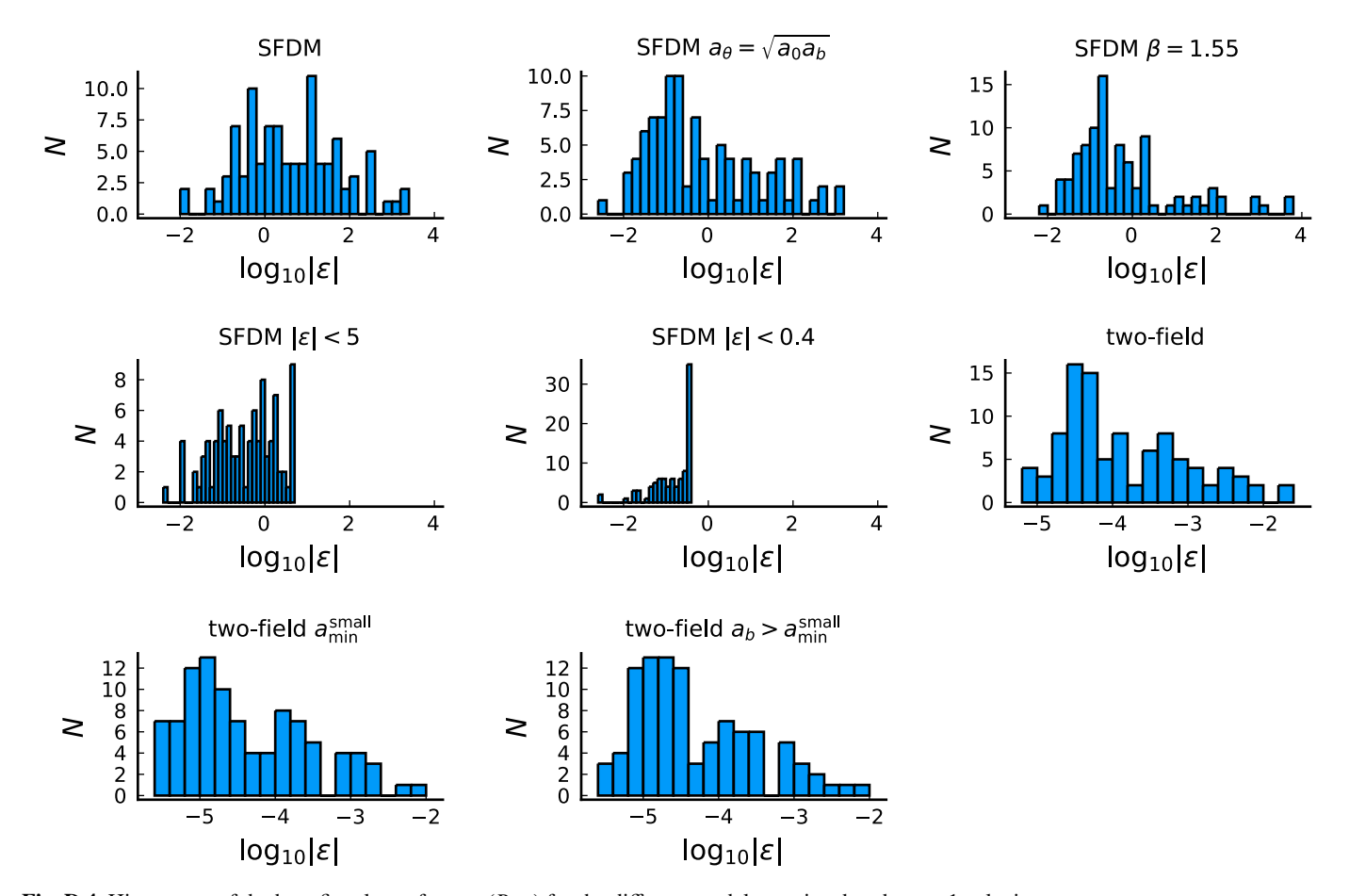


Fig. D.4. Histograms of the best-fit values of $\varepsilon = \varepsilon_*(R_{\rm mid})$ for the different models restricted to the q=1 galaxies.

elsewhere. The $|\varepsilon|$ in $10^7(1 + |\varepsilon|)$ is to help the χ^2 -minimizing fit algorithm to find small $|\varepsilon|$. In this fit, all galaxies are restricted to stay in the proper MOND limit $|\varepsilon| \ll 1$ of SFDM.

This works, but only for galaxies that are not too large. The restriction $|\varepsilon| < 0.1$ is impossible to satisfy for many larger galaxies. Our fitting procedure did not find any fit for 38 out of the 169 SPARC galaxies (i.e., 38 galaxies end up with $\chi^2 > 10^7$). This is not unexpected since our estimate $\varepsilon_* \gtrsim 0.1 + 0.4 \cdot (r/18\,\mathrm{kpc} - 1)$ from Eq. A.19 rules out $|\varepsilon| < 0.1$ for many larger galaxies. Indeed, Fig. D.5, top, shows that the galaxies that cannot be fit with $|\varepsilon| < 0.1$ tend to be those with $R_{\rm mid} \gtrsim 15\,\mathrm{kpc}$.

Since we set $\chi^2 = 10^7 (1 + |\varepsilon|)$ when the condition $|\varepsilon| < 0.1$ was not satisfied, our fitting algorithm actually minimized $|\varepsilon|$ until it satisfied $|\varepsilon| < 0.1$. Thus, we can get the minimum possible $|\varepsilon|$ for each galaxy where $|\varepsilon| < 0.1$ could not be satisfied. The results are shown in Fig. D.5, bottom. We see that many galaxies only barely fail to satisfy the condition $|\varepsilon| < 0.1$. Indeed, if we allowed $|\varepsilon|$ up to 0.4, almost all galaxies could be fit.

Of course, 0.4 is not that small, so it is debatable whether or not a value $|\varepsilon| = 0.4$ still counts as the proper MOND limit $|\varepsilon_*| \ll 1$. Here, we do not dwell on this point. However, we did redo our fit with the condition $|\varepsilon| < 0.1$ replaced by the condition $|\varepsilon| < 0.4$. As expected, we then obtained a fit for almost all galaxies. We did not find a fit for only four galaxies. Thus, if by "proper MOND limit" we mean $|\varepsilon| < 0.1$, SFDM's proper MOND limit does not work for lager galaxies. But if we allow $|\varepsilon|$ up to 0.4. it might.

for lager galaxies. But if we allow $|\varepsilon|$ up to 0.4, it might. The resulting best-fit χ^2 CDF is shown in Fig. D.1. In Fig. D.6, we show the changes in χ^2 between the "SFDM $|\varepsilon|$ < 0.4" fit and the unrestricted SFDM fit. The resulting χ^2 values tend to be worse than for the unrestricted SFDM fit, but generally still acceptable. Indeed, they are quite similar to those of the MOND fit (see the CDF in Fig. D.1).

For some galaxies, the condition $|\varepsilon| < 0.4$ can barely be satisfied. After satisfying this condition they have basically no freedom left to actually fit the observed rotation curve data and they end up with very bad χ^2 . Specifically, there are seven galaxies with $\varepsilon > 0.38$ and $\chi^2 > 100$. Since these are hardly useful in assessing the M/L_* required in SFDM, we separately list the M/L_* results with these galaxies excluded in Tables D.2 and D.1. We also exclude them in Fig. D.6.

Somewhat surprisingly, some galaxies even have a better best-fit χ^2 with the $|\varepsilon| < 0.4$ restriction than without (see Fig. D.6). Some of these are just very slightly better than the previous best fit. For two galaxies it improves by more than 15%, specifically by 46% for NGC 1090 and by 19% for NGC 2683. For all galaxies with an improved χ^2 , the corresponding best-fit M/L_* changes by less than 10%. These differences are insignificant for our purposes. They just show that our fitting algorithm is not perfect and does not always find the very best χ^2 .

If we exclude the galaxies with a bad χ^2 because they can only barely satisfy $|\varepsilon| < 0.4$ as described above, the resulting averaged stellar mass-to-light ratios are between 4% and 11% smaller than for the MOND fit. The numerical details depend on the averaging procedure and the cut of galaxies. We discuss the resulting M/L_* values in more detail in Appendix D.2.4.

An alternative to the proper MOND limit $|\varepsilon_*| \ll 1$ is the pseudo-MOND limit discussed in Appendix B.2. At $\varepsilon_* = O(1)$

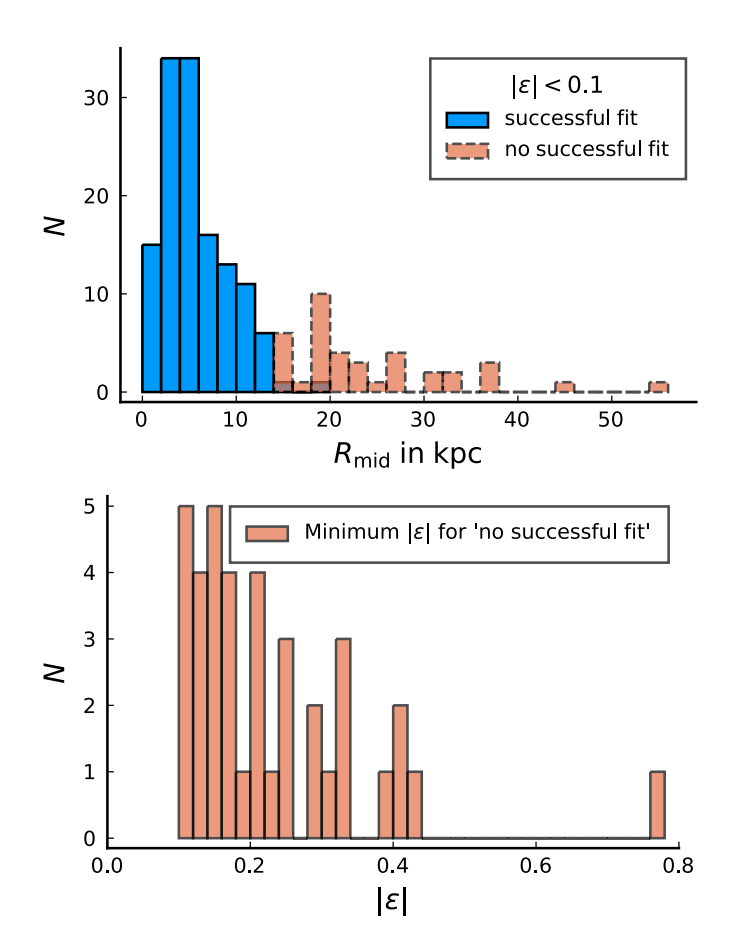


Fig. D.5. Fit results illustrating the ability of galaxies to satisfy the MOND limit condition $|\varepsilon| \ll 1$. Top: Histograms of the radius $R_{\rm mid}$ for galaxies where we did (blue) and did not (red) find a fit with the restriction $|\varepsilon| < 0.1$. We see that only smaller galaxies tend to be able to satisfy the condition $|\varepsilon| < 0.1$, consistent with the simple estimate $\varepsilon_* \gtrsim 0.1 + 0.4 \cdot (r/18\,{\rm kpc} - 1)$ from Eq. A.19. Bottom: Minimum possible $|\varepsilon|$ for the galaxies where we could find no fit with $|\varepsilon| < 0.1$. We see that many only barely fail to satisfy $|\varepsilon| < 0.1$, and we can get a fit for almost all galaxies with $|\varepsilon| < 0.4$.

(for $\beta=2$), the phonon acceleration a_{θ} is still numerically close to its MOND limit value $\sqrt{a_0a_b}$ although it does not satisfy a MOND-like equation (see Fig. A.1, left). To test this regime, we redid the SFDM fit with ε restricted to $|\varepsilon|<5$. This is the model shown as "SFDM $|\varepsilon|<5$ " in, for example, Table D.1 and Fig. D.2. Allowing values of $|\varepsilon|$ up to 5 allows the phonon acceleration a_{θ} to deviate by up to about 5% from its MOND limit value $\sqrt{a_0a_b}$ (at $R=R_{\rm mid}$) (see Fig. A.1). The resulting χ^2 values and stellar mass-to-light ratios are roughly comparable to those of the $|\varepsilon|<0.4$ fits. As always, the numerical details depend on the choice of galaxies and on whether we average using the median or the mean.

Thus, fitting the SPARC data does not require $\varepsilon_* \gg 1$ (i.e., it does not require going outside the MOND limit). Both the proper MOND limit and the pseudo-MOND limit also give reasonable χ^2 values. In this case, the averaged M/L_* is a bit smaller than in standard MOND models. In Appendix D.2.4, we discuss the M/L_* of these fits in more detail.

D.2.4. Trends of M/L_* with galaxy type

We now come back to the question of why SFDM does not necessarily need a smaller averaged M/L_* compared to MOND.

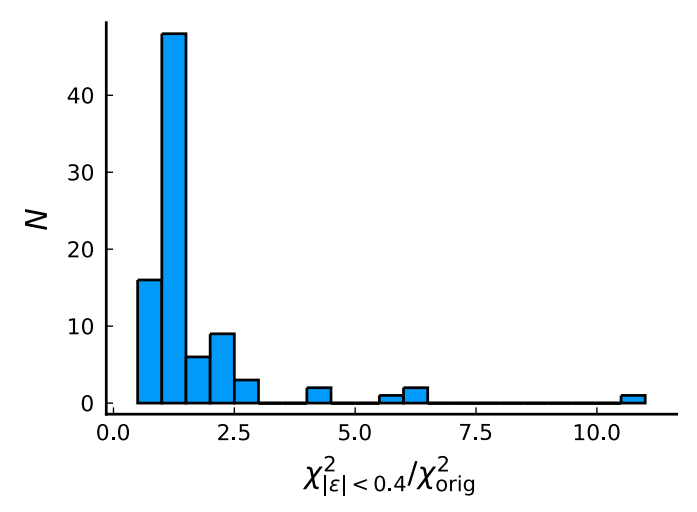


Fig. D.6. Histogram of the change in best-fit χ^2 values for the q=1 galaxies when switching from the unrestricted SFDM fit to that with the restriction $|\varepsilon| < 0.4$. This is excluding the galaxies that only barely satisfy $|\varepsilon| < 0.4$ and therefore have a bad χ^2 , i.e., excluding galaxies with $\varepsilon > 0.38$ and $\chi^2 > 100$.

Above, we already identified one reason, namely that many galaxies are not in the MOND limit $|\varepsilon_*| \ll 1$. But this is not the whole story, as we will now explain. To this end, we consider the fits with the MOND limit enforced as introduced in the previous subsection. This excludes effects from going outside the MOND limit.

In Appendix B.1, we argued that the MOND limit of SFDM likely requires a systematically smaller M/L_* than MOND only for high-acceleration galaxies. Galaxies with smaller accelerations may even require a larger M/L_* than MOND. The main reason is that SFDM has a smaller value of a_0 than MOND, which becomes important at small accelerations. If this is true, having a smaller or larger Q_* in SFDM is not just a property of the model but also a property of the galaxy sample. An example of this is Fig. 5, which shows the best-fit Q_* of each galaxy in the SFDM $|\varepsilon|$ < 0.4 model relative to the best-fit Q_* for MOND as a function of the observed flat rotation velocity $V_{\rm flat}$. A larger $V_{\rm flat}$ is associated with larger accelerations. Indeed, large $V_{\rm flat}$ values are where SFDM systematically gives smaller Q_* than MOND. Similarly, a smaller gas fraction and a larger surface brightness are associated with larger accelerations. The effective surface brightness Σ_{eff} and the ratio $M_{HI}/L_{[3.6]}$, a proxy for gas fraction, of each galaxy are also part of SPARC. And indeed, Fig. D.7 shows that SFDM has a systematically smaller M/L_* than MOND for galaxies with a large Σ_{eff} and a small $M_{HI}/L_{[3.6]}$.

To further test our understanding, we redid the MOND fit but using both the interpolation function v_{θ} instead of v_{e} (see Appendix B.1) and the smaller value a_{0}^{SFDM} of a_{0} . This should give fits qualitatively similar to those of the MOND limit of SFDM. Indeed, we verified that the resulting best-fit M/L_{*} show similar trends with, for example, V_{flat} as SFDM. As we explain in Appendix B.1, the different shape of the interpolation function is responsible for the systematically smaller M/L_{*} at large accelerations. The smaller a_{0} value is responsible for the fact that this is not true at smaller accelerations. Thus, in a MOND model with the SFDM-like interpolation function v_{θ} but with the larger a_{0} value a_{0}^{MOND} , we would expect to see a smaller M/L_{*} consistently across all accelerations. To test this, we redid the MOND fit with the interpolation function v_{θ} but keeping the larger value a_{0}^{MOND} of a_{0} . And indeed, this gives a consistently smaller M/L_{*}

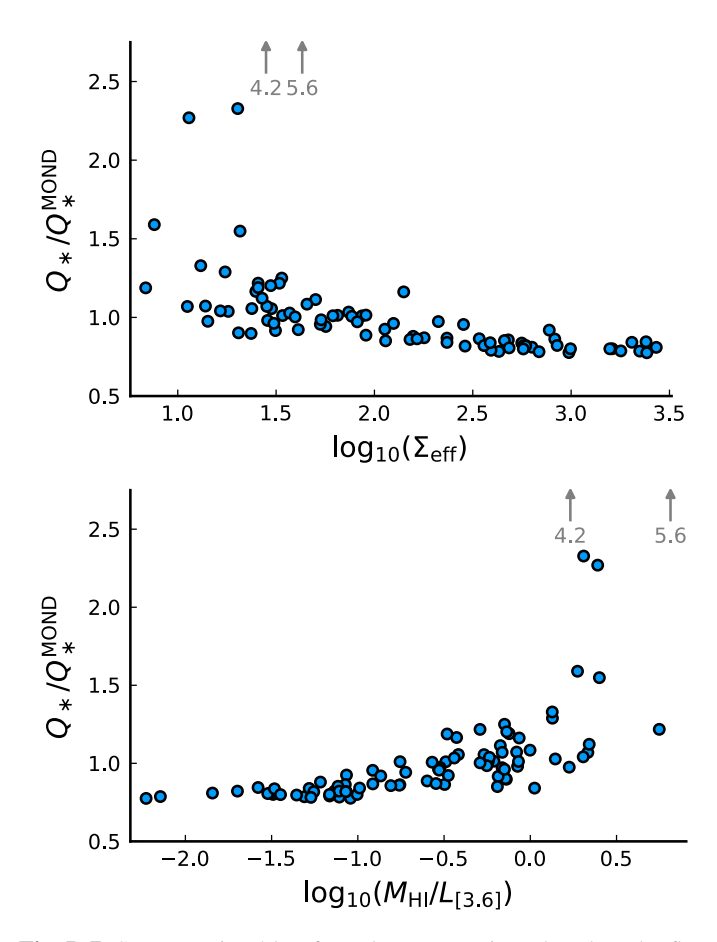


Fig. D.7. Same as Fig. 5 but for galaxy properties other than the flat rotation curve velocity, $V_{\rm flat}$. Top: For the effective surface brightness, $\Sigma_{\rm eff}$. Bottom: For $M_{HI}/L_{[3.6]}$.

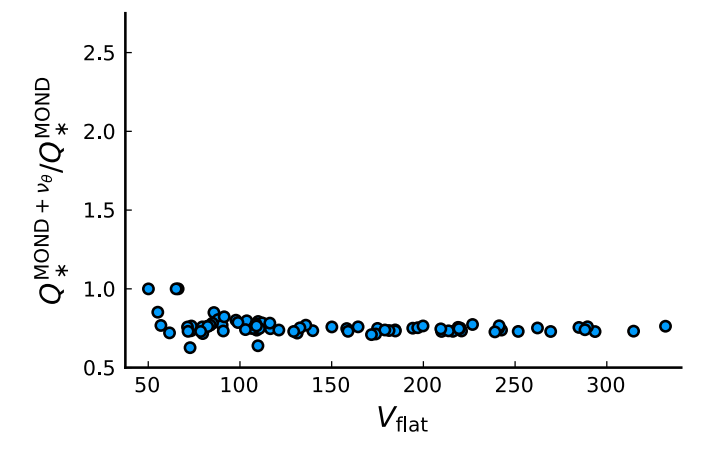


Fig. D.8. Same as Fig. 5 but for MOND fits that use the SFDM-like interpolation function, ν_{θ} , instead of ν_{e} and keeping the larger value a_{0}^{MOND} of a_{0} (rather than using the smaller value, a_{0}^{SFDM}).

than in MOND. There is no clear trend with, for example, $V_{\rm flat}$ (see Fig. D.8).

Trends of the stellar M/L in the [3.6] micron band with galaxy properties are not expected from SPS models (Schombert et al. 2019). This disfavors SFDM, especially compared to MOND, which does not show such trends. If anything, one expects the opposite trend: more massive galaxies should have higher mass-to-light ratios than dwarfs, especially in optical bands.

More precisely, when we do not normalize Q_* to $Q_*^{\rm MOND}$, our fitting procedure reproduces the SPS expectations for neither MOND nor SFDM. But this is a consequence of our simplistic fitting procedure. More sophisticated fits do reproduce the SPS expectations for MOND (McGaugh 2004). Moreover, since our simple fitting procedure is suited to identify relative differences between MOND and SFDM, we expect the trends in $Q_*/Q_*^{\rm MOND}$ to be robust. It is unlikely that these would be mitigated by a more sophisticated fitting procedure. That is, we expect that this conflict between SFDM and SPS expectations is real.

Figures 5 and D.7 not only show that SFDM has a systematically small Q_* for large accelerations. They also show that there is more scatter in $Q_*/Q_*^{\rm MOND}$ at smaller accelerations. One reason for this scatter is that many of the small-acceleration galaxies are gas-dominated. In gas-dominated galaxies, the formal best-fit value for the stellar mass-to-light ratio (i.e., Q_*) may not mean much, since a_b is relatively independent of Q_* . This allows for more scatter in Q_* .

D.2.5. The Milky Way

Hossenfelder & Mistele (2020) find that SFDM requires about 20% less baryonic mass than standard MOND models to fit the Milky Way rotation curve at $R \leq 25$ kpc. Specifically, it requires about 20% less baryonic mass than the MOND model from McGaugh (2019). This is a significantly larger difference than what we find, on average, for the SPARC galaxies (see Tables D.1 and D.2). Here, we confirm and discuss this result.

To confirm the result of Hossenfelder & Mistele (2020), we fitted the Milky Way with the same method we used for the SPARC galaxies. For this, we used ρ_b and $V_{\rm obs}$ as in Hossenfelder & Mistele (2020). The $V_{\rm obs}$ data based on Portail et al. (2017) that is used in Hossenfelder & Mistele (2020) for $R \leq 2$ kpc does not come with error bars. As a simple way to still get a result, we assumed an error of 5 km/s for these $V_{\rm obs}$ data points. For easier comparison to the SPARC fits, we rescaled the stellar disk and bulge densities such that stellar mass-to-light ratios of 0.5 (for the stellar disk) and 0.7 (for the bulge) correspond to the baryonic mass model used in McGaugh (2019). That is, the factor 10^{f_Y} tells us how much less stellar mass SFDM uses compared to the standard MOND model from McGaugh (2019). We found a best-fit χ^2 of 2.69, a best-fit Q_* of 0.79, and a best-fit ε of 4.37. This confirms the estimate from Hossenfelder & Mistele (2020) of about 20% less baryonic mass compared to standard MOND. This fit stays roughly within the pseudo-MOND limit $\varepsilon_* = O(1)$. With the best-fit parameters, ε_* stays below 15 at R < 25 kpc. Thus, the phonon acceleration cannot be much suppressed and cannot allow for an increased M/L_* , in contrast to galaxies at $\varepsilon_* \gg 1$ (see Appendix D.2.2).

The Milky Way's a_b ranges from about 10^{-9} m/s² to about $10^{-10.8}$ m/s² at R < 25 kpc for the best-fit parameters. These are relatively large. So, from the discussion in Appendix D.2.4, a smaller M/L_* than in MOND is what one would expect.

D.2.6. SFDM model parameters

Above, we used the fiducial parameter values from Berezhiani et al. (2018) and kept them fixed during the fitting procedure. Here, we discuss whether our conclusions could be changed by adjusting these parameters.

Our calculation does not depend on each of the four parameters, α , Λ , m, and β , separately. We need only the combinations

$$a_0 = \frac{\alpha^3 \Lambda^2}{M_{\rm Pl}}, \qquad \beta, \qquad \frac{m^2}{\alpha}.$$
 (D.1)

This can be seen directly from the SFDM Lagrangian (Berezhiani & Khoury 2015) by rescaling the phonon field, $\theta \to \theta (\alpha \Lambda/M_{Pl})^{-1}$. It also follows from $(\Lambda m^3)^2 = a_0 (m^2/\alpha)^3 M_{Pl}$.

First, the acceleration scale a_0 . To reproduce MOND, a_0 must be close to $10^{-10} \,\mathrm{m/s^2}$. Still, we could choose the same value as in standard MOND rather than the somewhat smaller value that Berezhiani et al. (2018) chose. This would give M/L_* values that are smaller than those for MOND for all galaxies, not just the small-acceleration ones (see Appendix D.2.4), at least as long as the superfluid's gravitational pull stays negligible. That is, SFDM would give M/L_* values similar to our "MOND ν_θ " fit (see Appendix D.2.4). These are relatively small. To get closer to M/L_* values as expected from SPS modeling, one would have to change not only the value of a_0 but also the form of the interpolation function ν_θ . This might be possible by adjusting the Lagrangian, that is, by changing what is usually called the function P(X) in superfluid low-energy effective field theories. Exploring this is beyond the scope of this paper.

One effect of the parameter β is that it controls the phonon force outside the proper MOND limit $|\varepsilon_*| \ll 1$ (see Appendix B.2). For one example ($\beta = 1.55$), we explicitly explored the effect of a different value of β (see Appendix D.2.2). Still, it is better not to tune this parameter for better fits to the data. This is because the value of β and the form of the finite-temperature corrections it is supposed to represent are completely ad hoc. So they might turn out to be unphysical. It is better to not rely too sensitively on any specific value of β for the fits.

The combination m^2/α multiplies both ε_* and the superfluid's energy density $\rho_{\rm SF}$. One motivation to change m^2/α is to make $|\varepsilon_*|$ small in order to allow more galaxies to reach SFDM's proper MOND limit $|\varepsilon_*| \ll 1$ (see Appendix A.1.2). The problem with this is that then $\rho_{\rm SF} \propto (m^2/\alpha) \cdot f_\beta(\varepsilon_*)$ becomes small as well. Indeed, in this case the problem regarding strong lensing described in Appendix D.4 becomes even worse. Conversely, making m^2/α larger in order to solve the strong lensing tension means even fewer galaxies can reach the MOND limit $|\varepsilon_*| \ll 1$. For example, increasing m^2/α by a factor of 10 would give $\varepsilon_* \gtrsim 0.1 + 0.41(r/1.8\,{\rm kpc}-1)$ from Eq. (A.19). Then, only the smallest galaxies could reach the proper MOND limit.

An adjusted function P(X) might invalidate this argument since this function determines not only the phonon force but also the superfluid's energy density in SFDM. But, again, this is beyond the scope of the present work.

To sum up, adjusting the SFDM model parameters might change some of our conclusions regarding the best-fit M/L_* values, but probably not in a way that is completely satisfactory from the perspective of SPS models. Moreover, we expect that the tradeoff between having MOND-like rotation curves and producing sufficient strong lensing described in Appendix D.4 remains.

D.2.7. Thermal radius check

We assumed that all SPARC rotation curve data points of a given galaxy lie within this galaxy's superfluid core. This is necessary for one of the main motivations behind SFDM, namely to automatically reproduce MOND-like rotation curves without having to adjust the boundary condition separately for each galaxy. The superfluid phase ends at the very latest when ρ_{SF} reaches zero.

Thus, we discarded solutions where ρ_{SF} vanishes inside the V_{obs} data points, as discussed in Appendix C.2.2.

But this may not be sufficient since the superfluid phase may end even before $\rho_{\rm SF}$ reaches zero. Consider, for example, the simplest estimate for the radius where the superfluid phase transitions to the non-superfluid phase, the so-called thermal radius R_T (Berezhiani et al. 2018). According to this estimate, the superfluid phase corresponds to

$$\Gamma > t_{\rm dyn}^{-1} \,, \tag{D.2}$$

where Γ is the local self-interaction rate and $t_{\rm dyn}$ is the dynamical time. Here, $\Gamma = (\sigma/m) \, \mathcal{N} \, v \, \rho$, where σ is the self-interaction rate, $\mathcal{N} = (\rho/m)(2\pi/mv)^3$ is the Bose-degeneracy factor, and v is the average velocity of the particles. Following Berezhiani et al. (2018), we take $\sigma/m = 0.01 \, \mathrm{cm}^2/\mathrm{g}$ and $t_{\rm dyn} = R/v$.

As a simple check, we evaluated the quantity $\Gamma/t_{\rm dyn}^{-1}$ for each galaxy at the last V_{obs} data point at R_{max} for the SFDM best fits. We found that 31 of 169 galaxies violate the condition $\Gamma > t_{\rm dyn}^{-1}$ at R_{max} . In principle, we should discard these solutions, just as we discard solutions where $ho_{\rm SF}$ reaches zero before $R_{\rm max}$. Here, we do not do this. The reason is that the condition $\Gamma > t_{\rm dyn}^{-1}$ is quite ad hoc. For example, the value of σ/m is chosen ad hoc and not derived from an underlying Lagrangian. Also, the transition radius derived from $\Gamma = t_{\rm dyn}^{-1}$ can, in general, differ wildly from the transition radius derived from the so-called NFW matching procedure (Berezhiani et al. 2018; Hossenfelder & Mistele 2020) where the density and pressure are matched to those of an NFW halo for a fixed NFW concentration parameter, as discussed in Mistele (2021). This makes any particular choice for discarding solutions based on the thermal or NFW matching somewhat arbitrary.

We avoid this arbitrariness by discarding solutions only based on the criterion that $\rho_{\rm SF}$ must be positive. Still, this means we do not discard some solutions that we maybe should discard. This might affect our M/L_* results. To get a rough idea of possible effects due to this, we also show our results for M/L_* in Table D.1 and Table D.2 with the 31 galaxies violating $\Gamma > t_{\rm dyn}^{-1}$ excluded, labeled as "thermal ok." Often, this does not significantly change the M/L_* fit results, though it does give a larger M/L_* for example for the SFDM model.

Overall, we expect that actually enforcing the rotation curve data to lie within the superfluid phase does not significantly change our M/L_{\ast} results. But keep in mind that there is a considerable theoretical uncertainty around the transition from the superfluid to the non-superfluid phase. We stress that the tension with strong lensing (see Appendix D.4) is not affected by this uncertainty, because there we anyway choose the transition radius to maximize the resulting total dark matter mass.

D.3. The RAR implied by the SFDM best fits

We show the RAR (i.e., the relation between a_b and $a_{\rm tot}$) implied by our SFDM fits for the q=1 galaxies in Fig. D.9. For each galaxy, we show one data point for each radius with a SPARC rotation curve data point $V_{\rm obs}$. As expected, the fit restricted to the proper MOND limit ($|\varepsilon| < 0.4$) shows a tight relation with almost no scatter. The unrestricted fit deviates from this in two ways. First, it produces significantly more scatter. Second, it systematically puts more data points below the relation implied by the proper MOND limit fit (i.e., it puts more data points at larger a_b , smaller $a_{\rm tot}$, or both). Of course, outside the MOND limit of SFDM, there is no guarantee that one ends up with a

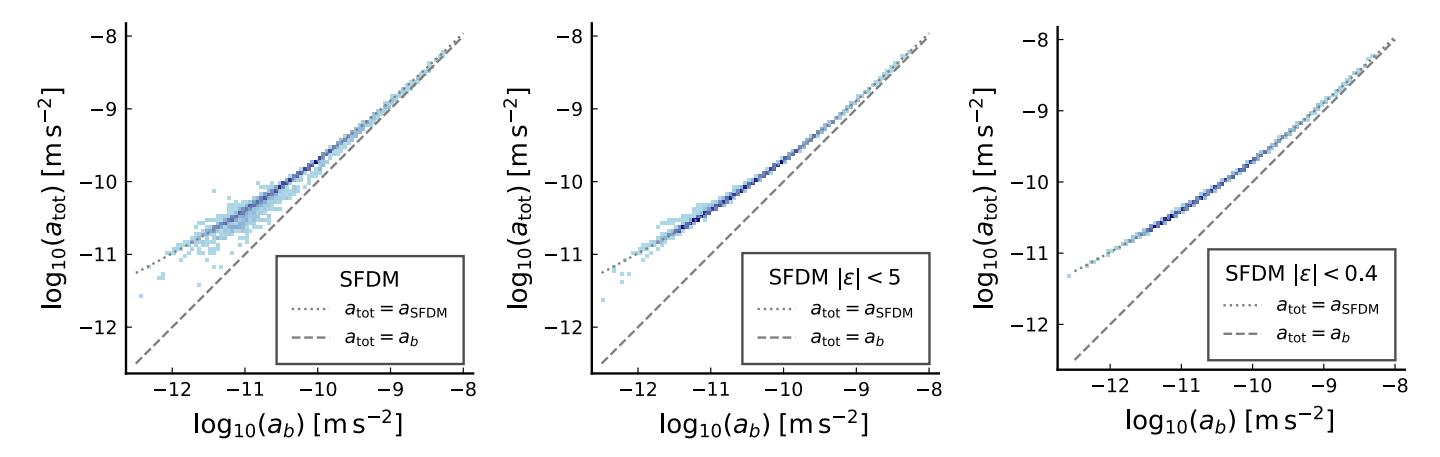


Fig. D.9. RAR of the q=1 galaxies implied by our SFDM fits for the unrestricted fit (left), the fit restricted to the pseudo-MOND limit ($|\varepsilon| < 5$, middle), and the fit restricted to the proper MOND limit ($|\varepsilon| < 0.4$, right). Each panel also shows the RAR implied by MOND with the SFDM-like interpolation function v_{θ} and $a_0 = 0.87 \cdot 10^{-10} \,\text{m/s}^2$, i.e., $a_{\text{SFDM}} = a_b \, v_{\theta}(a_b/a_0)$ (dotted gray line) and by Newtonian gravity with no dark matter (dashed gray line). For the $|\varepsilon| < 0.4$ fit we exclude the galaxies that only barely satisfy $|\varepsilon| < 0.4$ and therefore have a bad χ^2 , i.e., we exclude galaxies with $\varepsilon > 0.38$ and $\chi^2 > 100$.

MOND-like RAR. Still, we can understand in more detail why our unrestricted fits look the way they do.

One contribution to the increased scatter is as follows. The observed rotation curves contain some scatter from observational uncertainties. Our unrestricted SFDM fits match these observed rotation curves more closely than the fits restricted to the MOND limit (see, e.g., Fig. D.6). Thus, overfitting the noise in the observational data may, at least partly, explain the increased scatter in the RAR implied by our unrestricted fits.

We can also identify a possible cause for the systematic deviation from a MOND-like RAR. Namely, some observed rotation curves can be matched more closely outside the MOND limit (i.e., with a large $|\varepsilon_*|$). As discussed in Appendices B.2 and D.2.2, going outside the MOND limit allows for larger M/L_* : a large $|\varepsilon_*|$ makes $a_{\rm tot}$ smaller, which must be countered by a larger M/L_* . These larger M/L_* values explain why the RAR implied by our unrestricted SFDM fit puts significantly more data points below the tight RAR from the MOND limit than above it. Since this mechanism affects only some galaxies and since it affects different galaxies differently, this likely also contributes to the increased scatter.

When comparing the RAR implied by our fits to the actually observed RAR, one should keep in mind that, as mentioned above, observations always add scatter on top of what an underlying theory predicts. So, for example, if our unrestricted SFDM best fits are the ground truth, the observed RAR should contain even more scatter than what Fig. D.9, left, shows. At least if one ignores that some of the scatter in Fig. D.9, left, already reflects the scatter in the observed rotation curve data due to overfitting. The result may be even more scatter than what one obtains in actual observations with the simple prescription $(M/L_*)_{\rm disk} = 0.5$ and $(M/L_*)_{\rm bulge} = 0.7$ (Lelli et al. 2017b). Since SFDM aims to explain this observational fact, one might reject our unrestricted fit results purely on theses grounds.

Still, the objective of our fits was to match the observed rotation curve data, not to get a tight RAR. So our fit results do not directly imply that a non-tight RAR is an intrinsic property of going outside the MOND limit of SFDM. It may still be possible to get a tight RAR even outside the MOND limit. However, as discussed in Sect. 2, for this one would have to carefully adjust the boundary condition ε for each galaxy. Then, one must rely on galaxy formation to always pick the right values. This is con-

trary to the aim of SFDM to explain scaling relations such as the RAR without having to resort to the details of galaxy formation.

D.4. Tension with strong lensing in SFDM

The proper MOND limit $|\varepsilon_*| \ll 1$ of SFDM is useful for fitting rotation curves due to its MOND-like phonon force. Above, we saw that most SPARC rotation curves can be reasonably fit with the proper MOND limit $|\varepsilon_*| \ll 1$. At least if we count values of $|\varepsilon_*|$ as large as 0.4 as still satisfying $|\varepsilon_*| \ll 1$. But for certain other observables, such as strong lensing, the phonon force plays no role. This is because the observation of GW170817 requires that the phonon force does not affect photons (Hossenfelder & Mistele 2019; Sanders 2018; Boran et al. 2018). Thus, the strong lensing signal is produced only by the standard gravitational pull of the mass of the baryons and the superfluid, not by the phonon force.

As a consequence, the MOND limit of SFDM has a serious problem, because the superfluid's energy density is too small to produce significant lensing. Specifically, assuming the whole superfluid core to be in the MOND limit $|\varepsilon_*| \ll 1$, a rough upper bound is (see Appendix A.1.3)

$$\frac{M_{200}^{\rm DM}}{M_b} < \frac{1}{\sqrt{2\pi}} \frac{9}{4} \left(1 - \frac{\beta}{3} \right)^3 \left(\frac{m^2}{\alpha} \right)^3 \frac{\sqrt{a_0^3 M_b}}{\rho_{200}^2} = 0.9 \cdot \left(\frac{M_b}{10^{10} \, M_\odot} \right)^{1/2}, \tag{D.3}$$

where we assumed the numerical parameter values from Berezhiani et al. (2018). Producing sufficient strong lensing and a superfluid core in the MOND limit seem to be mutually exclusive. Choosing different parameter values may help, especially a larger m^2/α . But this would imply that fewer galaxies can reach the MOND limit $|\varepsilon_*| \ll 1$, as discussed in Appendix D.2.6.

This conclusion can, in principle, be avoided if the superfluid core is in the MOND limit only at smaller radii (where rotation curves are measured), but not at larger radii (where part of the lensing signal comes from). But even in this case there are limits on how large $M_{200}^{\rm DM}/M_b$ can be. This is because, given that we have $|\varepsilon_*| \ll 1$ at relatively small radii, the superfluid's energy density cannot be arbitrarily large at larger radii. Here, we check whether or not the SPARC galaxies can possibly have

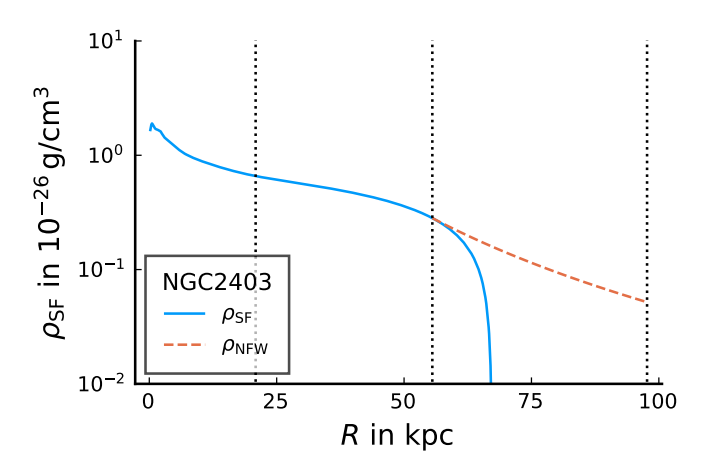


Fig. D.10. Dark matter energy density for NGC 2403 giving the largest possible $M_{200}^{\rm DM}$ compatible with a rotation curve in the MOND limit ($|\varepsilon| < 0.4$). The energy density is that of $\rho_{\rm SF}$ (solid blue line) for $r < r_{\rm NFW}$ and that of an NFW $1/r^3$ tail at larger radii (dashed red line). The two contributions are matched to each other at a radius $r_{\rm NFW}$, which is chosen to maximize $M_{200}^{\rm DM}$. This is for $(M/L_*)_{\rm disk} = 0.5$ and $(M/L_*)_{\rm bulge} = 0.7$ and gives $M_{200}^{\rm DM} = 9.8 \cdot 10^{10} \, M_{\odot}$. The dotted vertical lines denote $R_{\rm max}$, $r_{\rm NFW}$, and r_{200} .

a sufficiently large M_{200}/M_b for strong lensing, if we assume the proper MOND limit for the rotation curves.

Specifically, for each galaxy, we will find the largest possible value $M_{200,\rm max}^{\rm DM}$ of $M_{200}^{\rm DM}$ that is compatible with a rotation curve in the proper MOND limit. For the requirement that the rotation curve is in the proper MOND limit we impose $|\varepsilon| < 0.4$ as above.

In SFDM one usually assumes that the superfluid ends at a radius r_{NFW} beyond which the energy density is that of an NFW halo (Berezhiani & Khoury 2015; Berezhiani et al. 2018; Hossenfelder & Mistele 2020). For simplicity, we assumed the NFW profile $\rho_{NFW}(r)$ to be proportional to $1/r^3$ at the radii of interest, that is to say, we continued the superfluid density with an NFW tail instead of a full NFW profile. We do not expect this to significantly affect our results (Hossenfelder & Mistele 2019). The usual procedure for matching the superfluid density to the NFW profile is heuristic and not derived from first principles (Berezhiani et al. 2018; Mistele 2021). To be independent of the details of this matching procedure we matched the NFW density $ho_{
m NFW}$ to the superfluid density $ho_{
m SF}$ at a radius $r_{
m NFW}$ that is chosen to maximize $M_{200}^{
m DM}$. This gives the most conservative upper bound for $M_{200}^{\rm DM}$. We restricted $r_{\rm NFW}$ only in two ways. First, we assumed a positive superfluid energy density within the superfluid core, which implies that r_{NFW} is smaller than the radius r_m where ρ_{SF} vanishes. Second, we assumed all rotation curve data points to be within the superfluid core. Thus, we also restricted

 r_{NFW} to be larger than R_{max} . This is illustrated in Fig. D.10. To get the largest possible M_{200}^{DM} compatible with our constraints, we scanned values of ε in $(\varepsilon_{*\mathrm{min}}, 0.4)$ and values of r_{NFW} in (R_{max}, r_m) and recorded the largest M_{200}^{DM} as an upper bound $M_{200,\mathrm{max}}^{\mathrm{DM}}$. For a given ε and r_{NFW} we calculated M_{200}^{DM} by solving the equation

$$\frac{4\pi}{3}\rho_{200}r_{200}^3 = M_{\rm SF}(r_{\rm NFW}) + 4\pi r_{\rm NFW}^3 \rho_{\rm SF}(r_{\rm NFW}) \ln \left(\frac{r_{200}}{r_{\rm NFW}}\right) \quad ({\rm D}.4)$$

for r_{200} and then plugging the result into $M_{200}^{\rm DM}=(4\pi/3)\rho_{200}r_{200}^3$. We calculated $M_{\rm SF}(r)$ as $-(\hat{\mu}_{\rm SF}'(r)/m)(r^2/G)$. For some galaxies, it is not possible to solve the $\hat{\mu}_{\rm SF}$ equation with $|\varepsilon|<0.4$, if we

require a positive ρ_{SF} up to the last rotation curve data point. Such galaxies are excluded in the results shown below.

For the baryonic mass distribution we used the same values $(M/L_*)_{\rm disk}=0.5$ and $(M/L_*)_{\rm bulge}=0.7$ for all galaxies. These may not give the best fit to the measured rotation curves for all galaxies. However, here we are not interested in the fit to the rotation curve data, but in whether or not it is possible to have, at the same time, both a rotation curve in the proper MOND limit and sufficient $M_{200}^{\rm DM}$ for strong lensing. The precise value of M/L_* is irrelevant for this.

We can simplify the scanning procedure a bit. Namely, Fig. D.13 and Fig. D.14 suggest that increasing the boundary condition $\varepsilon \equiv \varepsilon_*(R_{\rm mid})$ increases $\varepsilon_*(r)$ at all radii, not just at $R_{\rm mid}$. We verified this numerically for various galaxies and boundary conditions. Here, we assumed that this is true in general. Consequences of this are that a larger boundary condition ε implies an everywhere larger superfluid energy density and a larger radius r_m where this energy density reaches zero. Therefore, for a fixed $r_{\rm NFW}$, the quantity $M_{200}^{\rm DM}$ is a monotonically increasing function of ε . Thus, we can simplify our scanning procedure by always setting $\varepsilon = 0.4$ and scanning only values of $r_{\rm NFW}$ in $(R_{\rm max}, r_m)$. For this, we used Mathematica's NMaximize function with its default options.

It can happen that the NFW radius $r_{\rm NFW}$ is bigger than the radius r_{∞} up to which we numerically solved for $\hat{\mu}_b$ (usually 100 kpc; see Appendix C.1). In this case, we must continue $\hat{\mu}_b$ beyond r_{∞} since solving the $\hat{\mu}_{\rm SF}$ equation requires $\hat{\mu}_b$ and a_b up to $r_{\rm NFW}$. For simplicity, we continued $\hat{\mu}_b$ beyond r_{∞} assuming spherical symmetry and zero baryonic energy density at $r > r_{\infty}$,

$$\frac{\hat{\mu}_b(r > r_\infty)}{m} = \frac{\hat{\mu}(r_\infty)}{m} - a_{b,R}(r_\infty)r_\infty^2 \left(\frac{1}{r_\infty} - \frac{1}{r}\right). \tag{D.5}$$

This implies $a_b(r > r_\infty) = a_{b,R}(r_\infty)r_\infty^2/r^2$. We expect errors due to this to not significantly change our results.

Below we need the total baryonic mass M_b of each galaxy. We adopt

$$M_b \equiv 0.5 \cdot (L_{[3.6]} - L_{\text{bulge}}) + 0.7 \cdot L_{\text{bulge}} + 1.4 \cdot M_{\text{HI}},$$
 (D.6)

where $L_{[3.6]}$, L_{bulge} , and M_{HI} are taken directly from SPARC. They denote the total [3.6] luminosity, the total bulge luminosity, and the HI mass, respectively. The stellar luminosities are weighted by their respective mass-to-light ratio. The factor 1.4 in front of the HI mass is to take into account helium and molecular hydrogen (McGaugh et al. 2020).

We show the results in Fig. 6. We see that large ratios $M_{200}^{\rm DM}/M_b$ are easier to reach for galaxies with relatively small baryonic masses M_b . In part, this is due to the factor $1/M_b$ in $M_{200}^{\rm DM}/M_b$. For strong lensing, relatively large baryonic masses are relevant. To illustrate this, we also show the best-fit values from the SFDM strong lensing analysis from Hossenfelder & Mistele (2019) in Fig. 6. These lensing galaxies tend to have $M_b \gtrsim 10^{11}\,M_\odot$ and $M_{200}^{\rm DM}/M_b \gtrsim 1000$. In contrast, the SPARC galaxies with $M_b > 10^{11}\,M_\odot$ almost

Indeed, a violation of this would imply that the boundary value problem is nonunique, contrary to what we already implicitly assumed in our calculations above, where we assumed that a value $\varepsilon_*(R_{\rm mid})$ uniquely specifies a solution. The reason is the following. If a larger boundary condition $\varepsilon_*(R_{\rm mid})$ gives a smaller $\varepsilon_*(r)$ at some radius $r=r_l$, then by continuity there must be a radius r_x between $R_{\rm mid}$ and r_l where the solutions $\varepsilon_*(r)$ for two different boundary conditions have the same value. Thus, the boundary value problem with boundary conditions imposed at $r=r_x$ is nonunique.

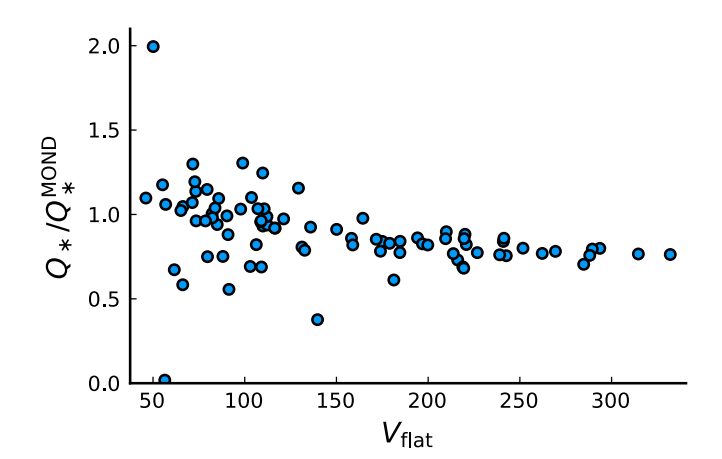


Fig. D.11. Same as Fig. 5 but for two-field SFDM.

all have $M_{200}^{\rm DM}/M_b < 10$ when restricted to have rotation curves in the MOND limit (i.e., when restricted to $|\varepsilon| < 0.4$). This is a stark contrast. The SPARC galaxies do not reach baryonic masses quite as large as the lensing galaxies from Hossenfelder & Mistele (2019). But from Fig. 6, it seems clear that the trend goes into the wrong direction: The larger the galaxy, the smaller the ratio $M_{200,\rm max}^{\rm DM}/M_b$ (assuming $|\varepsilon| < 0.4$).

Thus, it seems that a rotation curve in the MOND limit and sufficient dark matter for strong lensing are indeed mutually exclusive in standard SFDM. A caveat is that the galaxies in the SPARC sample are not ellipticals, in contrast to the lensing sample used in Hossenfelder & Mistele (2019). One might think that, for a given M_b , the maximum possible $M_{200}^{\rm DM}$ is not sensitive to the details of the baryonic mass distribution since the main contributions to $M_{200}^{\rm DM}$ come from large radii where, to a first approximation, only the total M_b plays a role. However, we impose the condition $|\varepsilon|$ < 0.4 at relatively small radii $R = R_{\text{mid}}$ where the details of the baryonic mass distribution may still matter. Indeed, the sensitivity of $M_{200,\mathrm{max}}^{\mathrm{DM}}$ to these details is reflected in the scatter in Fig. 6 (see also the end of Appendix D.6). Still, even being generous with this scatter, it seems unlikely that the difference in galaxy type explains why the SPARC galaxies restricted to $|\varepsilon| < 0.4$ cannot reach larger values of $M_{200}^{\rm DM}/M_b$. Also, Fig. 6 suggests that for $M_{200}^{\rm DM}/M_b$ values closer to those required for strong lensing (when restricting to $|\varepsilon|$ < 5 instead of $|\varepsilon|$ < 0.4) there is less scatter (i.e., less sensitivity to the baryonic mass distribution beyond the total M_b).

This suggests that strong lensing galaxies cannot have their inner parts (where rotation curves or velocity dispersions are measured) be in the proper MOND limit $|\varepsilon_*| \ll 1$. This is not in direct contradiction with measurements. Indeed, Hossenfelder & Mistele (2019) successfully fitted strong lensing data in SFDM. But one cannot easily keep the key idea of SFDM that the inner parts of galaxies are always in the proper MOND limit. Either one has to give up this key idea or one has to postulate that it does not apply to strong lensing galaxies for some reason.

D.5. M/L_* in two-field SFDM

By construction, the phonon acceleration in two-field SFDM should almost always be close to $\sqrt{a_0a_b}$ (Mistele 2021). The superfluid's Newtonian gravitational pull can be comparable to that of standard SFDM (Mistele 2021). Thus, we expect the fit

results for two-field SFDM to be close to that of the SFDM $a_{\theta} = \sqrt{a_0 a_b}$ model discussed above.

This should be true at least for the stellar mass-to-light ratios and the best-fit χ^2 . The results for $f_{M_{\rm DM}}$ may be not as close since the superfluid halo's shape is different. We discuss the superfluid halo in more detail below.

As expected, the best fits for two-field SFDM are almost all in the $|\varepsilon_*| \ll 1$ limit so that their phonon force a_θ is close to $\sqrt{a_0a_b}$. This is shown in Fig. D.4. Only for two galaxies (NGC 6789, UGC 07232) does ε_* become larger than 0.1. Its largest values is 0.36 for NGC 6789.

The averaged best-fit stellar mass-to-light ratios and the best-fit χ^2 can be found in Table D.1, Table D.2, and Fig. D.12. As expected, these are almost identical to those of the SFDM $a_\theta = \sqrt{a_0 a_b}$ model discussed above.

Two-field SFDM gives a systematically smaller M/L_* than MOND only for high-acceleration galaxies, not for low accelerations, just as standard SFDM (see Sect. 5.1 and Appendix D.2.4, and see Fig. D.11 for an example).

D.5.1. The minimum acceleration

In two-field SFDM, the equilibrium on galactic scales is stable only for phonon accelerations above a certain minimum acceleration. This minimum acceleration depends on the value of the field $\hat{\mu}/m$. Assuming $|\varepsilon_*| \ll 1$, as is usually the case, stability requires

$$a_b \left(10^7 \frac{\hat{\mu}}{m} \right)^2 > \bar{a} \,, \tag{D.7}$$

where \bar{a} is one of this model's parameters. Often, $\hat{\mu}/m$ is on the order of 10^{-7} on galactic scales. Thus, roughly, stability requires

$$a_b \gtrsim \bar{a}$$
 . (D.8)

When $\hat{\mu}/m$ is smaller, the instability sets in earlier. Mistele (2021) chose $\bar{a}=10^{-12}\,\mathrm{m/s^2}$ so that this model does not predict standard MOND-like behavior for dwarf spheroidals that may start to deviate from MOND-like behavior around $a_b\sim 10^{-12}\,\mathrm{m/s^2}$ (Lelli et al. 2016). In our two-field SFDM fit we adopted this value of \bar{a} .

For galaxies violating Eq. (D.7), we should in principle model what happens beyond the minimum acceleration in two-field SFDM. Here, we did not do this for two reasons. First, this regime is not well-understood. Second, we are interested in the MOND regime inside the superfluid core. Modeling the behavior beyond the minimum acceleration will not help us understand whether or not the MOND regime of two-field SFDM requires a larger or smaller M/L_* than standard MOND models.

Still, 98 of 169 SPARC galaxies violate the condition Eq. (D.7) at $R_{\rm max}$. For these galaxies, our fit is not meaningful since it relies on an unstable equilibrium. This is expected for the dwarf spheroidals with a_b around 10^{-12} m/s². But the 98 galaxies violating Eq. (D.7) include many more galaxies, also at $a_b \gg \bar{a}$. We will have to deal with this one way or another.

To further explore this, we redid the two-field SFDM fit with the much smaller value $\bar{a}=10^{-14}\,\mathrm{m/s^2}$. This is listed as "two-field $a_{\mathrm{min}}^{\mathrm{small}}$ " in our tables and figures. The resulting M/L_* and χ^2 values are almost identical to those of the previous two-field SFDM fit. But still 71 galaxies violate Eq. (D.7).

Thus, Eq. (D.7) is often not violated because a_b is smaller than \bar{a} but because $\hat{\mu}/m$ is smaller than 10^{-7} . A small $\hat{\mu}/m$ corresponds to a small superfluid mass $M_{\rm DM}$. Indeed, Fig. D.3 shows

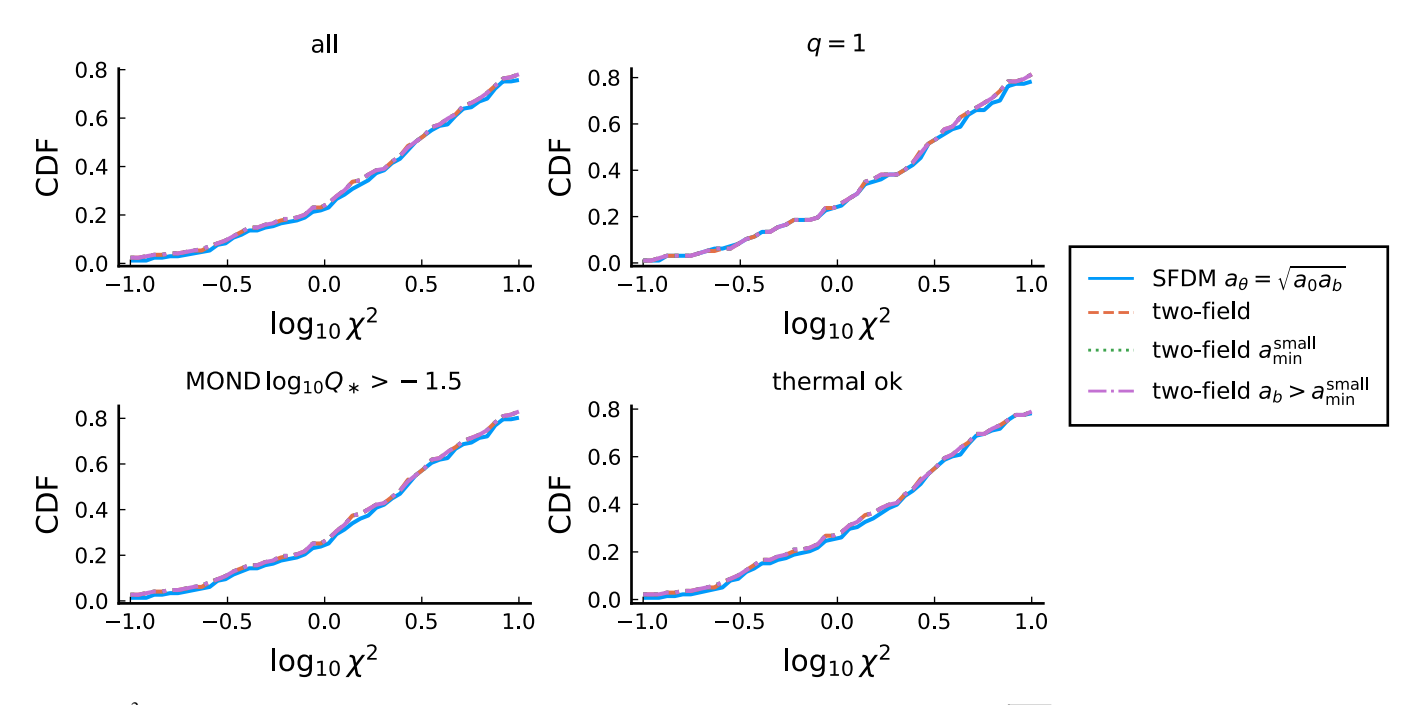


Fig. D.12. χ^2 CDFs for the different two-field models and galaxy cuts. Also shown is the SFDM $a_{\theta} = \sqrt{a_0 a_b}$ fit for comparison.

that many galaxies have a smaller $f_{M_{\rm DM}}$ in two-field SFDM compared to standard SFDM, for both \bar{a} values discussed above.

This raises two questions. The first is whether two-field SFDM really needs to go to small $\hat{\mu}/m$ to fit the SPARC data, thus often violating Eq. (D.7). The second is why standard SFDM tends to end up at larger $f_{M_{\rm DM}}$ values than two-field SFDM.

D.5.2. Origin of the small $f_{M_{\rm DM}}$ values in two-field SFDM

The best-fit χ^2 and M/L_* are almost identical for the two-field SFDM fits and for the standard SFDM fit with $a_\theta = \sqrt{a_0 a_b}$. But the superfluid halos of two-field SFDM reach much smaller masses than those in standard SFDM (see Fig. D.3). For example, there are no galaxies at $f_{M_{\rm DM}} < -2.3$ in any standard SFDM fit, but many such galaxies in two-field SFDM. The only relevant difference between two-field SFDM and the SFDM $a_\theta = \sqrt{a_0 a_b}$ model is the difference in their $\rho_{\rm SF}$. Thus, this different superfluid energy density must be the reason for the qualitative difference in $f_{M_{\rm DM}}$. Here, we explain this in more detail.

As discussed above, we enforced a positive superfluid energy density at radii smaller than the last rotation curve data point (i.e., $\rho_{SF} > 0$ at $R \le R_{max}$). The difference between standard and two-field SFDM regarding small dark matter masses boils down to what this condition implies.

Consider first two-field SFDM. In two-field SFDM, the superfluid energy density vanishes when $\hat{\mu}/m=0$. Equivalently, when $\varepsilon_*=0$. Typically, $\hat{\mu}/m$ is a decreasing function of galactocentric radius.³ Thus, whenever the condition $\rho_{\rm SF}>0$ is fulfilled at the largest radius of interest, $R=R_{\rm max}$, it is fulfilled at all radii of interest (i.e., at $R\leq R_{\rm max}$). In a given galaxy, a smaller superfluid mass $M_{\rm SF}(R)$ at some radius, for example at $R=R_{\rm max}$,

implies a smaller $\hat{\mu}/m$ everywhere in the superfluid core (not just at $R=R_{\rm max}$). Indeed, different superfluid masses just correspond to adding a term $\sin(r/r_0)/r$ with a different prefactor to $\hat{\mu}_{\rm SF}$; see Appendix C.4. Thus, if we go to smaller and smaller $f_{M_{\rm DM}}$, we go to smaller and smaller $\hat{\mu}/m$. At some point, $\hat{\mu}/m$ will become negative at $R=R_{\rm max}$. Then, we are at the minimum possible $f_{M_{\rm DM}}$ allowed by our condition $\rho_{\rm SF}>0$.

The condition $\rho_{SF} > 0$ at $R = R_{max}$ enforces a minimum possible mass also in standard SFDM. A difference is that the superfluid energy density in standard SFDM vanishes not at $\varepsilon_* = 0$ but at a negative value $\varepsilon_{*min} \approx -0.31$ (for $\beta = 2$). Using the definition of ε_* from Eq. (1), this constant negative lower bound on $\varepsilon_*(x)$ becomes a nonconstant lower bound $\hat{\mu}_{\min}(x)$ on $\hat{\mu}(x)$. This is illustrated in Fig. D.13 for NGC 2403. The top panel shows solutions $\hat{\mu}/m$ for various boundary conditions ε . The bottom panel shows ε_* for the same boundary conditions. Both panels also show the lower bounds on ε_* and $\hat{\mu}$, respectively, which ensure $\rho_{\rm SF} > 0$. For the smallest boundary condition value $\varepsilon = 0.08$ shown in Fig. D.13, both ε_* and $\hat{\mu}$ reach this lower bound at $R = R_{\text{max}}$. Thus, $\varepsilon = 0.08$ corresponds to the smallest possible superfluid mass that is allowed by the condition $\rho_{SF} > 0$. Lower superfluid masses would need ρ_{SF} to reach zero before $R = R_{max}$, which we do not allow. This is similar to as in two-field SFDM.

However, in contrast to two-field SFDM, this constraint at $R=R_{\rm max}$ is not the only constraint on superfluid masses in standard SFDM. In standard SFDM, having $\rho_{\rm SF}>0$ at $R=R_{\rm max}$ does not imply $\rho_{\rm SF}>0$ at smaller radii. The main issue is at R=0. This is illustrated in Fig. D.14 for DDO 168. For the smallest boundary condition value $\varepsilon=-0.06$ shown in Fig. D.14, at $R=R_{\rm max}$, both $\hat{\mu}/m$ and ε_* are not close to the minimum values that $\rho_{\rm SF}>0$ allows. However, at R=0, the minimum values are reached (i.e., $\rho_{\rm SF}$ vanishes). Thus, the boundary condition $\varepsilon=-0.06$ corresponds to the minimum possible $f_{M_{\rm DM}}$ allowed by our condition $\rho_{\rm SF}>0$. But now the constraint comes from R=0 rather than $R=R_{\rm max}$.

To understand this, consider small radii, $R \to 0$. At $R \to 0$, the field $\hat{\mu}$ reaches a finite value $\hat{\mu}(0)$. The Newtonian baryonic acceleration $|a_b(R)|$ goes to zero, typically $a_b \propto R$ for $R \to 0$.

³ This is always the case in spherical symmetry as long as ρ_{SF} is positive. Indeed, then $\hat{\mu}'(r)/m = -G(M_b + M_{SF})/r^2 < 0$. Here, we assumed spherical symmetry only for $\hat{\mu}_{SF}$, but not for $\hat{\mu}_b$. Thus, only $\hat{\mu}_{SF}$ is guaranteed to be a decreasing function of galactocentric radius, not the total $\hat{\mu}$. Still, the total $\hat{\mu}(R, z = 0)$ typically decreases as a function of R also in our case.

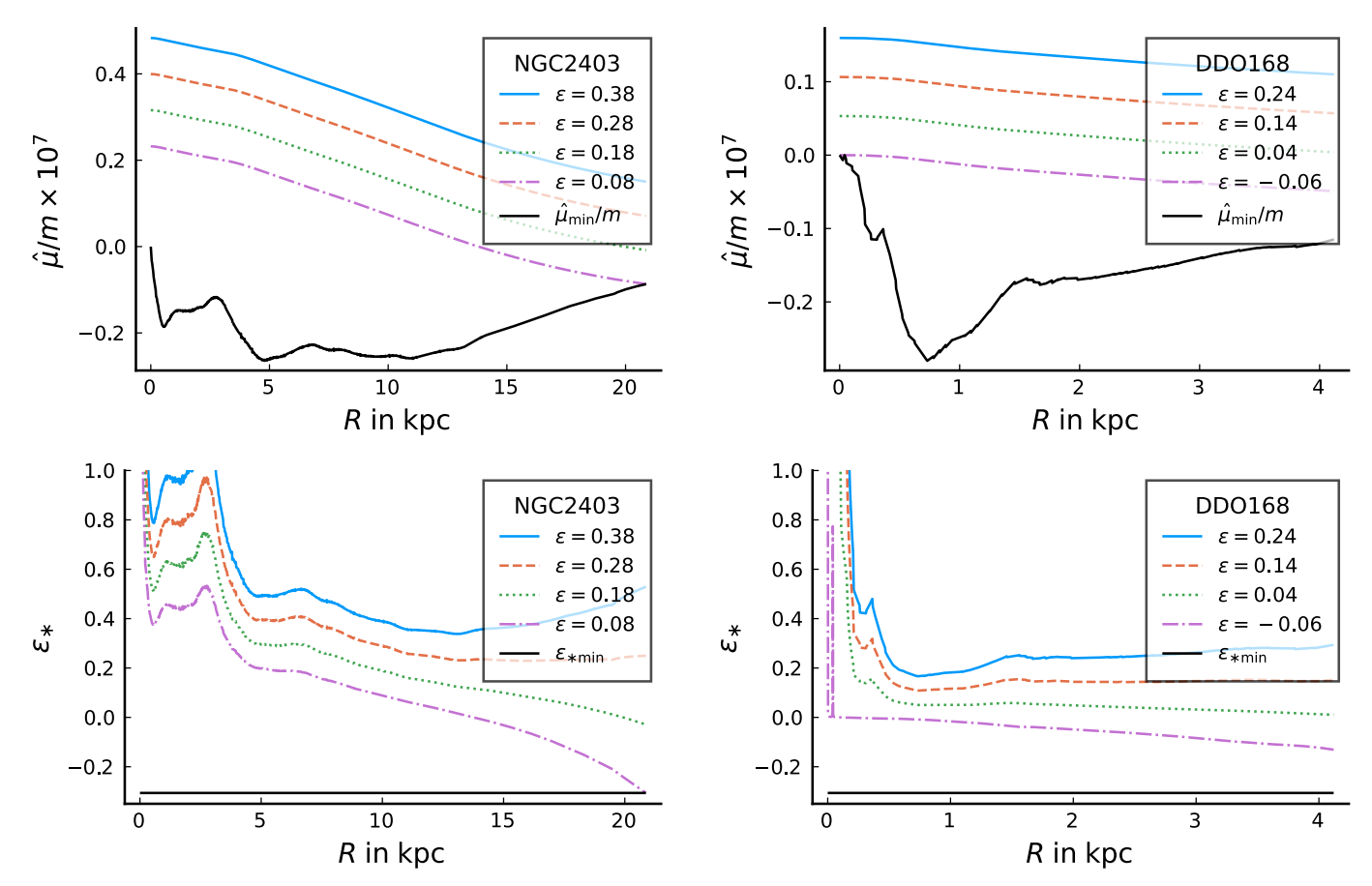


Fig. D.13. Solutions for $\hat{\mu}/m$ and ε_* for various boundary conditions, ε , for the galaxy NGC 2403 assuming the best-fit Q_* for SFDM. Top: Quantity $\hat{\mu}/m$ at z=0. The solid black line shows the minimum possible value of $\hat{\mu}/m$ allowed by the condition $\rho_{\rm SF}>0$ at each radius. The smallest boundary condition, $\varepsilon=0.08$, corresponds to the minimum possible dark matter mass for the given baryonic mass distribution. Smaller masses would require that the condition $\rho_{\rm SF}>0$ is violated before $R=R_{\rm max}$. Bottom: Same as the top panel but showing ε_* instead of $\hat{\mu}/m$. The minimum possible ε_* allowed by $\rho_{\rm SF}>0$ is a constant.

Thus, we have from the definition of ε_* Eq. (1)

$$\varepsilon_*(R \to 0) \propto \frac{\hat{\mu}(0)}{R} \to \pm \infty$$
 (D.9)

That is, ε_* tends to $\pm \infty$ with the sign being that of $\hat{\mu}(0)$. A positive ρ_{SF} requires $\varepsilon_*(0) \ge \varepsilon_{*\min}$. Thus, we must have

$$\hat{\mu}(0) \ge 0. \tag{D.10}$$

This condition $\hat{\mu}(0) > 0$ must also hold in two-field SFDM. But, in two-field SFDM, $\hat{\mu}(0) > 0$ follows from $\rho_{SF} > 0$ at $R = R_{max}$. This is because $\hat{\mu}$ is a decreasing function of radius and because $\rho_{SF} > 0$ requires $\hat{\mu} > 0$ even at $R = R_{max}$. So this adds nothing in two-field SFDM.

This is different in standard SFDM. A positive ρ_{SF} at $R=R_{\max}$ does not necessarily imply a positive $\hat{\mu}(0)$ and thus a positive ρ_{SF} at R=0. Since $\hat{\mu}$ is a decreasing function of radius, violating $\hat{\mu}(0)>0$ is possible only if $\hat{\mu}$ is negative already at $R=R_{\max}$. Consider this case where $\hat{\mu}$ is negative at $R=R_{\max}$. Since $\hat{\mu}$ decreases with radius, it can happen that $\hat{\mu}$ grows sufficiently between $R=R_{\max}$ and R=0 to become positive at R=0. In this case the condition $\hat{\mu}(0)>0$, corresponding to $\rho_{SF}>0$ at R=0, gives no additional constraint. However, this is

Fig. D.14. Same as Fig. D.13 but for DDO 168. The smallest boundary condition shown, $\varepsilon = -0.06$, again corresponds to the minimum possible mass allowed by $\rho_{\rm SF} > 0$. But now smaller masses would violate this condition at R = 0 instead of at $R = R_{\rm max}$.

not guaranteed to happen. When $\hat{\mu}$ does not grow sufficiently, the condition $\hat{\mu}(0) > 0$ gives an additional constraint. This is what happens for DDO 168 as illustrated in Fig. D.14.

This, then, is the reason why two-field SFDM allows smaller superfluid masses (i.e. smaller $f_{M_{\rm DM}}$) compared to standard SFDM. In both models, small superfluid masses correspond to $\rho_{\rm SF}$ close to zero. And in both cases one needs to be careful not to let this density become negative (or ill-defined) at $R=R_{\rm max}$. However, in standard SFDM, being close to $\rho_{\rm SF}=0$ implies a negative $\hat{\mu}$, and in this case there can be an additional constraint at R=0, as just discussed. This second constraint is absent in two-field SFDM where $\rho_{\rm SF}$ vanishes already at $\hat{\mu}=0$.

As mentioned above, this second constraint in standard SFDM occurs only when $\hat{\mu}$ does not grow sufficiently between $R=R_{\rm max}$ and R=0. We now make this more precise. The minimum allowed superfluid mass from the constraint at $R=R_{\rm max}$ corresponds to $\rho_{\rm SF}=0$ at $R=R_{\rm max}$. This constraint is present in both standard and two-field SFDM. Reaching this minimum mass implies

$$\hat{\mu}(R_{\text{max}}) = \varepsilon_{*\text{min}} \frac{\alpha M_{\text{Pl}} |\boldsymbol{a}_b(R_{\text{max}})|}{2m} \,. \tag{D.11}$$

A second constraint $\hat{\mu}(0) > 0$ from R = 0 is avoided whenever $\hat{\mu}$ grows between $R = R_{\text{max}}$ and R = 0 by at least

$$\hat{\mu}(0) - \hat{\mu}(R_{\text{max}}) > -\varepsilon_{*\text{min}} \frac{\alpha M_{\text{Pl}} |a_b(R_{\text{max}})|}{2m} \,. \tag{D.12}$$

As the example of DDO 168 (see Fig. D.14) shows, this is not always guaranteed in standard SFDM. But in some cases it is. Namely, as in Appendix C.2, we can write $\hat{\mu} = \hat{\mu}_b + \hat{\mu}_{SF}$. Both $\hat{\mu}_b$ and $\hat{\mu}_{SF}$ typically decrease with radius, with the amount they decrease being determined by the baryonic and superfluid mass, respectively. Once we know the baryonic mass distribution, we know a lower bound on how much the total $\hat{\mu}$ grows, independently of the superfluid energy density and the boundary condition ε . As a result, if the baryonic mass alone makes $\hat{\mu}$ grow sufficiently, we never get an additional constraint from $\hat{\mu}(0) > 0$. This is the case if

$$\hat{\mu}_b(0) - \hat{\mu}_b(R_{\text{max}}) > -\varepsilon_{*\min} \frac{\alpha M_{\text{Pl}} |\boldsymbol{a}_b(R_{\text{max}})|}{2m} \,. \tag{D.13}$$

Thus, more quantitatively, we claim that standard SFDM cannot get masses as low as two-field SFDM because Eq. (D.13) is often not satisfied. That is, there is an additional constraint from R=0 in standard SFDM that is not present in two-field SFDM. We expect that, without this constraint, galaxies would end up at smaller $f_{M_{\rm DM}}$ also in standard SFDM.

As a consequence, we expect that the galaxies that end up at very small $f_{M_{\rm DM}}$ in two-field SFDM but not in standard SFDM violate Eq. (D.13). To check this, we selected the 30 galaxies that have $f_{M_{\rm DM}} < -2.3$ in two-field SFDM. As mentioned above, no galaxies have such small $f_{M_{\rm DM}}$ in standard SFDM. For the most direct comparison against two-field SFDM we use the best-fit stellar M/L_* from the SFDM $a_\theta = \sqrt{a_0 a_b}$ fits. We find that these 30 galaxies all violate Eq. (D.13) so that they face an additional constraint in standard SFDM. This confirms our explanation why galaxies reach smaller $f_{M_{\rm DM}}$ values in two-field SFDM compared to standard SFDM.

D.5.3. Enforcing the minimum acceleration in two-field SFDM

In Appendix D.5.1, we saw that many best fits in two-field SFDM violate the minimum acceleration condition Eq. (D.7), even with a reduced \bar{a} value. The reason is that many galaxies end up at small $\hat{\mu}/m$, or, equivalently, at small superfluid masses corresponding to small $f_{M_{\rm DM}}$ (see Appendix D.5.2).

For small superfluid masses, the precise mass is often not important for fitting rotation curves since the corresponding $a_{\rm SF}$ is subdominant. Thus, it may be possible that we can find fits with sufficiently large $\hat{\mu}/m$ so that all galaxies satisfy the minimum acceleration condition without getting significantly worse fits. To check this, we redid the two-field SFDM fit with $\bar{a}=10^{-14}\,{\rm m/s^2}$ but with the minimum acceleration condition Eq. (D.7) enforced. That is, whenever this condition is violated we set $\chi^2=10^{10}$ so that our fit code goes elsewhere. We label this model "two-field $a_b>a_{\rm min}^{\rm small}$."

As we can see from Table D.1, Table D.2, and Fig. D.12, this

As we can see from Table D.1, Table D.2, and Fig. D.12, this gives almost identical results for the best-fit χ^2 and M/L_* values as the previous two-field SFDM fits. This shows that it is not necessary for two-field SFDM to violate the minimum acceleration condition. The small $\hat{\mu}/m$ values are not required to get a reasonable fit (see also Fig. D.3).

D.6. Tension with strong lensing in two-field SFDM

In two-field SFDM, the $|\varepsilon_*| \ll 1$ condition is almost always fulfilled so that the phonon force is almost always close to the MOND-like value $\sqrt{a_0a_b}$. So, in contrast to standard SFDM,

simultaneously being in the $|\varepsilon_*| \ll 1$ limit and producing a sufficient strong lensing signal is not a problem. However, in two-field SFDM, a small ε_* does not imply that $a_{\rm SF}$ is negligible. So two-field SFDM may still not be able to produce MOND-like rotation curves and sufficient strong lensing at the same time.

To check this, we calculated a maximum total dark matter mass $M_{200}^{\rm DM}$ in the same way as we did for standard SFDM in Appendix D.4. But instead of imposing $|\varepsilon| < 0.4$ we imposed

$$a_{\rm SF} < 0.3 (a_b + a_\theta)$$
 (D.14)

at $R = R_{\text{max}}$. For simplicity, we assumed $a_{\theta} = \sqrt{a_0 a_b}$, which is usually a good approximation. Then, Eq. (D.14) becomes

$$\frac{GM_{\rm DM}(R_{\rm max})}{R_{\rm max}^2} < 0.3 \cdot (a_b + \sqrt{a_0 a_b}). \tag{D.15}$$

To implement this numerically, we used $M_{\rm DM}(R_{\rm max})$ instead of $\varepsilon_*(R_{\rm mid})$ as a boundary condition. This translates to a boundary condition on $\hat{\mu}'_{\rm SF}(R_{\rm max})/m$ instead of on $\hat{\mu}(R_{\rm mid})/m$. We can still solve the two-field equations as described in Appendix C.4 with this modified boundary condition.

The value 0.3 is somewhat arbitrary. It is chosen to give a non-negligible but still subdominant $a_{\rm SF}$. There is a clear trade-off here. Larger values allow for larger total dark matter masses $M_{200}^{\rm DM}$ but also larger deviations from MOND-like rotation curves. Smaller values give more MOND-like rotation curves but also smaller total dark matter masses.

One way to find the largest possible $M_{200}^{\rm DM}$ compatible with the condition Eq. (D.15) is to just scan over all possible $M_{\rm DM}(R_{\rm max})$ satisfying the condition. But we do not have to do this here for the same reason we did not have to do it for standard SFDM (see Appendix D.4). Basically, since a larger $M_{\rm DM}(R_{\rm max})$ always gives a larger $M_{200}^{\rm DM}$.

Above, we considered different values of the parameter \bar{a} , which determines the minimum acceleration. Here, we use $\bar{a}=10^{-12} \, \mathrm{m/s^2}$. But the choice of \bar{a} does not actually affect the maximum M_{200}^{DM} we calculate since we keep r_0 and a_0 fixed. It only determines how small ε_* is since $m^2/\alpha \propto (\bar{a}/a_0)^{1/4}$. That is, it determines how well our approximation $a_\theta = \sqrt{a_0 a_b}$ works. Since, by construction, $|\varepsilon_*| \ll 1$ for any reasonable value of \bar{a} , this approximation works well for any reasonable \bar{a} .

The result is shown in Fig. 9 and discussed in Sect. 5.3. Comparing Fig. 9 for two-field SFDM and Fig. 6 for standard SFDM, there is less scatter in the derived relation between $M_{200,\text{max}}^{\text{DM}}$ and M_b for two-field SFDM. This is likely because this relation in two-field SFDM is less sensitive to the details of the baryonic mass distribution at a given total baryonic mass M_b . There are a few reasons for this. First, the superfluid energy density $\rho_{\rm SF}$ scales as $\sqrt{a_b}$ in standard SFDM (at least in the MOND limit $|\varepsilon_*| \ll 1$) but not in two-field SFDM. Second, we impose the condition $|\varepsilon|$ < 0.4 in standard SFDM at smaller radii $R = R_{\text{mid}}$ than $a_{SF}/(a_b + a_\theta) < 0.3$ in two-field SFDM, which we impose at $R = R_{\text{max}}$. There is less variation in the baryonic mass distribution at larger radii. Third, these conditions depend on different quantities. The left-hand side of $|\varepsilon|$ < 0.4 in standard SFDM scales as $\hat{\mu}/a_b$ while the left-hand side of $a_{SF}/(a_b + a_\theta) < 0.3$ in two-field SFDM scales as $M_{\rm SF}/\sqrt{a_b}$, at least at larger radii where $a_{\theta} \propto \sqrt{a_b}$ dominates. The acceleration $a_{\rm SF}$ depends only on $\hat{\mu}_{\rm SF}$, while $\hat{\mu}$ also depends on $\hat{\mu}_b$, which is much more sensitive to the details of the baryonic mass distribution. Similarly, $\sqrt{a_b}$ is less sensitive to these details than a_b .